Supplementary Information for

Relational reduction protects massless spin-2 modes in a programmable quantum network

Contents

Supplementary overview

This document gives the complete general protection theorems, the finite BCC realization, the controlled Gaussian quantum-coordinate correction, the exact finite-kernel matching results, the direct static branch, robustness analysis and the programmable protocol supporting the main Article. The general results require only a positive quantum chart, an exact relational complex with two-dimensional cohomology, a positive response on the quotient and a finite spectral representation. The BCC network supplies one explicit realization.

Theorem S0.1 (Summary protection and realization theorem)**.** *Let $V_0 \xrightarrow{G} V_1 \xrightarrow{Q} V_2$ be a finite exact complex with $QG = 0$ and $\dim(\ker Q/\operatorname{im} G) = 2$. If a positive quantum response descends to this cohomology, then any covariant representative differing by $Q^{\mathsf{T}}WQ$ has the same reduced two-mode dynamics. If the quantum chart has positive Legendre Hessian, its Gaussian Schur feedback preserves the kernel, masslessness and positive physical spectral measure. The finite BCC route/Gram/Julia model below realizes these hypotheses, has a direct inverse-distance static branch, and can be falsified by the five-qubit protocol of Sec. S11.2. A unique nonlinear Einstein completion is not required for these statements.*

S1 General relational protection theorems

S1.1 Exact complex and constraint-square equivalence

Let V_0, V_1, V_2 be finite-dimensional real Hilbert spaces and let

$$V_0 \xrightarrow{G} V_1 \xrightarrow{Q} V_2, \qquad QG = 0. \tag{S1}$$

Assume that G has closed image, Q has full row rank on the chosen incidence sector, and

$$\mathcal{H} = \ker Q/\operatorname{im} G, \qquad \dim \mathcal{H} = 2. \tag{S2}$$

After choosing the orthogonal gauge-fixed complement of $\operatorname{im} G$, the remaining space decomposes as

$$V_1^{\mathrm{gf}} = \mathcal{H} \oplus \operatorname{im} Q^{\mathsf{T}}. \tag{S3}$$

Let $K_H \succeq 0$ be supported on $\mathcal{H}$, and let $B, C \succ 0$ on V_2.

Theorem S1.1 (Relational constraint-square protection)**.** *The operators*

$$K_+ = K_H + Q^{\mathsf{T}}BQ, \qquad K_{\mathrm{cov}} = K_H - Q^{\mathsf{T}}CQ \tag{S4}$$

have identical reduced dynamics on $\mathcal{H}$. Their difference is

$$K_+ - K_{\mathrm{cov}} = Q^{\mathsf{T}}(B + C)Q, \tag{S5}$$

a positive quadratic form in the imposed constraint $Qh = 0$. If $K_H(p) = p^2 A + O(p^4)$ with $A \succ 0$, both representatives contain exactly two massless positive-norm modes.

Proof. For every $h \in \ker Q$, Eq. (S5) vanishes. The Euler–Lagrange equations of the two constrained actions differ by $Q^{\mathsf{T}}(B+C)Qh$ and by a corresponding redefinition of the algebraic multiplier enforcing $Qh = 0$. Quotienting by $\operatorname{im} G$ leaves the common restriction $K_H|_{\mathcal{H}}$. The stated low-momentum form then has two eigenvalues proportional to p^2 with positive leading matrix A. □

The theorem does not require the constraint rank to be one, the ambient dimension to be six, or the geometry to be BCC. Those properties enter only in the realization below.

S1.2 Gaussian Schur protection

Let $H_G \succ 0$ be the Legendre Hessian of a positive quantum chart and let $K \succeq 0$ be the occupied response. For a chart fluctuation δh coupled to the same source, consider

$$\Gamma^{(2)}[h, \delta h] = \frac{1}{2}\delta h^{\mathsf{T}} H_G \delta h + \frac{1}{2}(h + \delta h)^{\mathsf{T}} K (h + \delta h). \tag{S6}$$

Theorem S1.2 (Gaussian Schur protection)**.** *Integrating δh gives*

$$K_{\mathrm{red}} = K - K(H_G + K)^{-1}K. \tag{S7}$$

Then $K_{\mathrm{red}} \succeq 0$ and $\ker K_{\mathrm{red}} = \ker K$. On the support of K,

$$K_{\mathrm{red}}^{-1} = K^{-1} + H_G^{-1}. \tag{S8}$$

If $K(p) = p^2 A + O(p^4)$, then

$$K_{\mathrm{red}}(p) = p^2 A - p^4 A H_G^{-1} A + O(p^6), \tag{S9}$$

so the leading rank and masslessness are unchanged.

Proof. Equation (S7) is the Schur complement of the positive block Hessian of Eq. (S6). On the support of K, direct multiplication gives the parallel-sum identity (S8); the kernel statement follows by continuity on the orthogonal complement. Expanding the inverse in KH_G^{-1} gives Eq. (S9). □

Corollary S1.3 (Preservation of a positive spectral measure)**.** *Suppose the physical propagator $D(z) = K(z)^{-1}$ is meromorphic with simple real poles and positive-semidefinite residues, and $H_G^{-1}(z)$ is analytic in the spectral window. Then*

$$D_{\mathrm{red}}(z) = D(z) + H_G^{-1}(z) \tag{S10}$$

has exactly the inherited poles and residues and no new poles in that window. It may acquire zeros; those are antiresonances of the propagator, not new excitations.

S1.3 Randomized structural audit and failure boundary

We sampled 3,000 exact complexes with $\dim V_1 = 6$–12, constraint ranks 1–9 and positive-chart condition numbers $1, 10^2, \ldots, 10^{10}$. Gauge, physical and constraint subspaces were generated from random orthogonal frames. Positive response and chart matrices were sampled with log-uniform spectra. Every sample passed the exact-complex, two-dimensional-cohomology, constraint-square, positivity and Schur-kernel tests. The largest constraint-square residual was 4.13×10^{-16} and the largest complex residual was 7.37×10^{-16}.

A destructive control adds a component of G in the row space of Q. Physical-mode leakage then grows continuously with the normalized defect $\|QG\|/(\|Q\|\|G\|)$. The first 1% leakage occurs at drive parameter $\epsilon = 1.4193 \times 10^{-2}$, corresponding to complex defect 5.79×10^{-3}. Exactness is therefore a measurable protection condition, not a slogan.

A separate 1,000-member random Stieltjes ensemble had zero interlacing failures, zero negative-residue failures and zero new poles under analytic positive Schur feedback. The maximum parallel-sum propagator residual was 1.55×10^{-16}. These audits test numerical implementation of the algebraic theorems; they do not replace their proofs.

Table S1: Model-independent randomized audit. Each row contains 500 independently generated exact complexes.

Chart condition number	Samples	Joint pass fraction	Max. constraint-square residual
1	500	1.000	4.01×10^{-16}
10^2	500	1.000	3.71×10^{-16}
10^4	500	1.000	3.67×10^{-16}
10^6	500	1.000	4.12×10^{-16}
10^8	500	1.000	4.07×10^{-16}
10^{10}	500	1.000	3.22×10^{-16}

S2 Microscopic history model and hybrid status

This section gives every microscopic and relational ingredient used later. The construction should be read in the following order. A finite unitary moves route amplitudes on the BCC event graph. A recurrence coin opens a quasienergy gap. The four-port centered-Gram record provides a provisional classical geometry on which the quantum history depends. The relative-cofactor Julia link compares source and target geometry without an absolute reference coframe. Filling the negative-phase branch defines a Gaussian occupied state, whose closed-time-path determinant supplies the induced response. Finally, the event-section map and scalar condition specify which geometric variations are physical.

Definition S2.1 (Hybrid finite causal-cell model)**.** The model is the tuple

$$\mathfrak{M}_{\mathrm{hyb}} = (\Lambda_{\mathrm{BCC}}, \mathcal{H}_1, U_m, \mathcal{H}^{(K)}_{\mathrm{Gram}}, \widehat{\boldsymbol{g}}, \mathcal{M}_{\mathrm{Gram}}, \mathcal{J}_{\mathrm{rel}}, P_-, \mathcal{C}_{\mathrm{rel}}), \tag{S11}$$

where Λ_{BCC} is the event graph, $\mathcal{H}_1$ is the finite one-particle route/recurrence space, U_m is the parity-completed recurrence update, $\mathcal{H}^{(K)}_{\mathrm{Gram}}$ is a finite Gauss-invariant four-port Hilbert space at capacity cutoff K, $\widehat{\boldsymbol{g}}$ is a six-operator quantum Gram chart, $\mathcal{M}_{\mathrm{Gram}}$ is the positive centered-Gram mean-field manifold, $\mathcal{J}_{\mathrm{rel}}$ is the relative-cofactor Julia link, P_- is the occupied projector, and $\mathcal{C}_{\mathrm{rel}}$ is the event-section/scalar constraint complex. Route/recurrence variables, $\widehat{\boldsymbol{g}}$, and P_- are quantum. Their Gram expectation values define a classical saddle in $\mathcal{M}_{\mathrm{Gram}}$. The coframe, compatible connection, and $\mathcal{C}_{\mathrm{rel}}$ are not promoted to a full operator theory, but the leading Gaussian fluctuations of the Gram saddle and their feedback on the occupied response are integrated explicitly in Sec. S5.

The finite hybrid carrier space is the product

$$\mathcal{H}^{(K)}_{\mathrm{cell}} = \mathcal{H}_1 \otimes \mathcal{H}^{(K)}_{\mathrm{Gram}}. \tag{S12}$$

The calculation uses the mean-field factorization

$$\rho_{\mathrm{cell}} \approx \rho_J \otimes \rho_{\mathrm{occ}}[E(\bar{\mathcal{G}})], \tag{S13}$$

so the Gram sector supplies the collective coordinate while the route/recurrence sector supplies the displayed dynamical response. Section S5 relaxes the frozen-coordinate approximation at Gaussian order and gives the exact Schur-complement feedback. Non-Gaussian Gram–route entanglement remains outside the theorem.

Logical status of the variables. Here “derived” always means derived inside Definition S2.1, not established as a law of nature.

- **Route and recurrence amplitudes — finite quantum variables.** They evolve unitarily on the BCC graph; the displayed free one-particle model is exact.
- **Occupied projector P_- — Gaussian quantum state.** It selects filled histories and generates source, response, contact terms, thresholds, and noise. Non-Gaussian matter is open.
- **Quantum Gram chart $\widehat{g}$ — finite Gauss-invariant operators.** Their mean values and covariances are calculated on $\mathcal{H}^{(K)}_{\mathrm{Gram}}$. They make the collective source an expectation-value coordinate rather than an arbitrary six-component tensor.
- **Centered Gram record $\bar{\mathcal{G}}$ — Legendre-dual collective mean field.** It exactly reconstructs a positive spatial metric modulo a common rotation. Its identification with microscopic spacetime geometry remains provisional.
- **Coframe $E[\bar{\mathcal{G}}]$ — saddle representative of the quantum Gram field.** It is a square root used to couple and compare histories. The leading Gaussian fluctuations about this saddle are integrated exactly; no non-Gaussian path integral over E is supplied.
- **Connection ω — classical compatibility/source field.** It is used for Cartan transport and the first-order extension. No quantum measure over ω is supplied.
- **Constraint complex $\mathcal{C}_{\mathrm{rel}}$ — classical relational reduction.** It removes event-section representatives and one scalar direction. It is not an anomaly-free operator constraint algebra on a quantum-geometry Hilbert space.
- **Induced response — quantum effective action for classical sources.** The occupied history induces the quadratic physical stiffness. Any Einstein nonlinear completion is conditional on Sec. S6.3.

  There is no bare two-derivative gravitational kinetic coefficient:

$$Z^{\mathrm{bare}}_{\mathrm{EH}} = Z^{\mathrm{bare}}_{\mathrm{EC}} = 0. \tag{S14}$$

Equation (S14) does not turn the collective Gram field into a complete quantum spacetime. The quantum port algebra below supplies the coordinate and a locally invertible source–mean map. The classical mean field is the leading saddle, and Sec. S5 proves that its Gaussian correction preserves the physical quotient and spectral sign. The tensor stiffness is therefore generated by the occupied history rather than by an independent Einstein coefficient, while the remaining approximation is specifically non-Gaussian rather than permanently classical.

S2.1 Event graph, Weyl blocks, and recurrence unitary

The event graph is the Cayley graph of $\mathbb{Z}^3$ with the eight oriented BCC routes

$$\mathcal{R}_{\mathrm{BCC}} = \{(r_x, r_y, r_z) : r_i = \pm 1\}. \tag{S15}$$

At fixed dimensionless momentum $\boldsymbol{q}$, a Weyl block acts on $\mathbb{C}^2$. Write $c_i = \cos q_i$ and $s_i = \sin q_i$. For $\sigma = \pm 1$, define

$$d_\sigma = c_x c_y c_z + \sigma s_x s_y s_z, \tag{S16}$$

$$\boldsymbol{u}_\sigma = \big(s_x c_y c_z - \sigma c_x s_y s_z, -\sigma c_x s_y c_z - s_x c_y s_z, c_x c_y s_z - \sigma s_x s_y c_z\big). \tag{S17}$$

These obey $d_\sigma^2 + |\boldsymbol{u}_\sigma|^2 = 1$, so

$$W_\sigma(\boldsymbol{q}) = d_\sigma I_2 - i\boldsymbol{u}_\sigma \cdot \boldsymbol{\sigma} \tag{S18}$$

is unitary. The recurrence block acts on $\mathbb{C}^2_{\mathrm{Weyl}} \otimes \mathbb{C}^2_{\mathrm{rec}} \simeq \mathbb{C}^4$:

$$D_{\sigma,m}(\boldsymbol{q}) = \begin{pmatrix} \cos m\, W_\sigma(\boldsymbol{q}) & i \sin m\, I_2 \\ i \sin m\, I_2 & \cos m\, W_\sigma(\boldsymbol{q})^\dagger \end{pmatrix}, \qquad 0 < m < \frac{\pi}{2}. \tag{S19}$$

It is exactly unitary and has paired eigenphases satisfying

$$\cos \omega_\sigma(\boldsymbol{q}) = \cos m\, d_\sigma(\boldsymbol{q}). \tag{S20}$$

The Weyl blocks and their BCC locality follow the established QCA construction [9, 10]; the recurrence coupling and the occupied geometric history are the additional structures studied here. The parity-completed update is the direct sum

$$U_m(\boldsymbol{q}) = D_{+,m}(\boldsymbol{q}) \oplus D_{-,m}(\boldsymbol{q}), \tag{S21}$$

with equal occupation of the two BCC parity sectors. This cancels the parity-odd cubic term in the low-momentum scalar history. A finite capacity sector K may provide additional internal copies; the one-channel theorem sets that multiplicity to one and later replaces it by the invariant total oscillator strength $\mathcal{Z}_{\mathrm{occ}}$.

With event length a, tick τ, and $c = a/\tau$, the branch-free causal symbols

$$E_\sigma = \frac{\hbar}{\tau} \sin \omega_\sigma, \quad \Delta_c = \frac{\hbar}{\tau} \sin m, \quad \boldsymbol{p}_{c,\sigma} = \frac{\hbar}{a} \cos m\, \boldsymbol{u}_\sigma \tag{S22}$$

obey the exact finite-band shell

$$E_\sigma^2 = \Delta_c^2 + c^2 |\boldsymbol{p}_{c,\sigma}|^2. \tag{S23}$$

The parity-even route incidence used by the tensor response is

$$\rho_H(\boldsymbol{q}) = \frac{1}{8} \sum_{\boldsymbol{r} \in \mathcal{R}_{\mathrm{BCC}}} 4 \sin^2\!\left(\frac{\boldsymbol{r} \cdot \boldsymbol{q}}{2}\right) = 2\big(1 - \cos q_x \cos q_y \cos q_z\big), \tag{S24}$$

with

$$\rho_H = q^2 - \frac{1}{12} I_4 + O(q^6), \qquad I_4 = 3(q^2)^2 - 2 \sum_i q_i^4. \tag{S25}$$

S2.2 Provisional centered-Gram geometry

Let t_a be the four unoriented tetrahedral representatives of the BCC routes, normalized so $\sum_a t_a = 0$, and collect them as the rows of a 4×3 matrix T. A classical coframe representative $E \in GL^+(3)$ defines

$$q = E^T E, \qquad F(E) = \det(E) E^{-T}, \qquad C = F(E)^T F(E) = \det(q) q^{-1}. \tag{S26}$$

The observable local record is not E itself but the centered Gram matrix

$$\mathcal{G} = TCT^T, \qquad \mathcal{G}\mathbf{1} = 0. \tag{S27}$$

For a nondegenerate frame, $\mathcal{G}$ contains six independent components and determines q modulo a common $SO(3)$ rotation; the exact inverse is given in Section S4. Thus E is a convenient representative of a relational orbit. This paper establishes that the candidate coordinate acquires a positive induced tensor stiffness. It does not derive a quantum operator $\widehat{E}$, a quantum state of geometry, or a measure over $\mathcal{G}$.

The event scale a is likewise a conversion between graph separation and the collective coframe normalization. The primitive BCC coordinate cell has volume $4a^3$, but the physical event volume is written generally as

$$v_0 = \eta a^3, \tag{S28}$$

with $\eta = 4$ only in the primitive coframe convention. A dynamical derivation of η is not supplied.

S2.3 Quantum port-Gram algebra and the classical mean-field restriction

The classical Gram coordinate is tied to explicit quantum observables on a Gauss-invariant four-port register that shares the incidence labels of the route geometry. Give port $a = 1, \ldots, 4$ a Schwinger doublet a_{aA}, $A = \uparrow, \downarrow$, and define

$$\widehat{J}^i_a = \frac{1}{2} a^\dagger_{aA} (\sigma^i)_{AB} a_{aB}, \qquad [\widehat{J}^i_a, \widehat{J}^j_b] = i\delta_{ab}\epsilon^{ijk}\widehat{J}^k_a. \tag{S29}$$

The Gauss-invariant finite port space at even capacity cutoff K is

$$\mathcal{H}^{(K)}_{\text{Gram}} = \bigoplus_{N=0,2,\ldots,K} \text{Inv}_{SU(2)}\left[\mathcal{F}_N\left((\mathbb{C}^2)^{\oplus 4}\right)\right], \qquad \sum_{a=1}^{4} \widehat{\boldsymbol{J}}_a = 0. \tag{S30}$$

A convenient six-operator chart is

$$\widehat{\boldsymbol{g}} = (\widehat{\boldsymbol{J}}_1^2, \widehat{\boldsymbol{J}}_2^2, \widehat{\boldsymbol{J}}_3^2, \widehat{\boldsymbol{J}}_4^2, \widehat{\boldsymbol{J}}_1 \cdot \widehat{\boldsymbol{J}}_2, \widehat{\boldsymbol{J}}_1 \cdot \widehat{\boldsymbol{J}}_3). \tag{S31}$$

Gauss closure fixes the remaining pairwise products. For every density matrix ρ on this space, the full mean Gram matrix

$$\bar{\mathcal{G}}_{ab} = \text{Tr}\Big(\rho\, \widehat{\boldsymbol{J}}_a \cdot \widehat{\boldsymbol{J}}_b\Big) \tag{S32}$$

is centered and positive semidefinite because

$$\bar{\mathcal{G}}\mathbf{1} = 0, \qquad c_a c_b \bar{\mathcal{G}}_{ab} = \text{Tr}\left[\rho\left(\sum_a c_a \widehat{\boldsymbol{J}}_a\right)^2\right] \geq 0. \tag{S33}$$

When $\bar{\mathcal{G}}$ has rank three, Sec. S4 reconstructs a coframe representative $E[\bar{\mathcal{G}}]$ modulo a common rotation.

To show that six independent mean coordinates are genuinely available, introduce the finite source family

$$\rho_J = \frac{e^{-J_A \widehat{g}_A}}{Z[J]}, \qquad \bar{g}_A(J) = -\frac{\partial \ln Z}{\partial J_A}, \qquad \chi_{AB} = \frac{\partial^2 \ln Z}{\partial J_A \partial J_B} = \int_0^1 \mathrm{d}s\ \text{Tr}\Big(\rho_J^s\, \delta\widehat{g}_A\, \rho_J^{1-s}\, \delta\widehat{g}_B\Big). \tag{S34}$$

At $J = 0$ the state is proportional to the identity and this Kubo–Mori covariance reduces to the symmetrized trace covariance used in Appendix S14. The Legendre transform of $-\ln Z[J]$ defines a local collective effective potential for $\bar{\boldsymbol{g}}$. The hybrid approximation used in the rest of the article evaluates the route/recurrence determinant at the resulting classical mean coframe $E[\bar{\mathcal{G}}]$; it does not integrate over $\bar{\mathcal{G}}$ or include its quantum entanglement with the route sector.

Proposition S2.2 (Finite quantum origin of the collective Gram chart)**.** *For the explicit cutoff $K = 4$, the $N = 0, 2, 4$ Gauss-singlet sectors have dimensions 1, 6, and 20, so $\dim \mathcal{H}^{(4)}_{\text{Gram}} = 27$. In the maximally mixed Gauss state, the mean Gram matrix has diagonal entries $3/4$, off-diagonal entries $-1/4$, and eigenvalues $(0, 1, 1, 1)$. The six-by-six covariance χ of Eq. (S34) is strictly positive. Consequently $J \mapsto \bar{\boldsymbol{g}}$ is locally invertible, and the provisional classical coframe is a Legendre-dual mean field of explicit finite quantum port operators rather than an unconstrained external tensor.*

Proof. Direct Gauss projection gives the stated sector dimensions. The exact covariance matrix and its leading principal minors are displayed in Appendix S14; all six minors are positive, so Sylvester's criterion gives $\chi \succ 0$. The inverse-function theorem then gives local invertibility of the source–mean map. Positivity and centering of the mean Gram matrix follow from Eq. (S33). The proposition supplies a quantum collective-coordinate origin, not a quantum gravitational measure or dynamics for the coframe. □

S2.4 Relative-cofactor Julia link and ordered history

The cofactor

$$F(E) = \det(E)E^{-T} \tag{S35}$$

acts on oriented area elements rather than on line elements. This is the natural geometric object for the four closed ports, which behave as face or flux directions. An *absolute* cofactor $F(E)$ would still compare every event with a preferred identity frame. The source–target arrow instead uses the relative area map

$$R_{ts} = F(E_t)\, L_{ts}\, F(E_s)^{-1}, \tag{S36}$$

where L_{ts} is the compatible frame transporter; $L_{ts} = I$ in the flat induction calculation. If source and target have the same constant coframe, then $R_{ts} = I$ in their local orthonormal variables. For the symmetric split $E_\pm = e^{\pm h/2}E$,

$$F(E_+)F(E_-)^{-1} = e^{(\mathrm{Tr}\, h)I - h}. \tag{S37}$$

Thus the common background cancels before any momentum expansion. The strain h changes only the relation between the two endpoints.

Geometry also changes the amount of amplitude transmitted through a route. At route $\boldsymbol{r}$, the flat amplitude is

$$\alpha_{\boldsymbol{r}} = \cos m \cos\theta_{\boldsymbol{r}}, \qquad \theta_{\boldsymbol{r}} = \frac{\boldsymbol{r}\cdot\boldsymbol{q}}{2}, \tag{S38}$$

and the geometry-dependent contraction is $C_{\boldsymbol{r}} = \alpha_{\boldsymbol{r}} R_{ts}$. A contraction alone would lose norm into unrecorded channels. Its canonical Julia dilation restores exact unitarity by retaining the complementary amplitude:

$$\mathcal{J}(C) = \begin{pmatrix} C & (I - CC^\dagger)^{1/2} \\ (I - C^\dagger C)^{1/2} & -C^\dagger \end{pmatrix}, \qquad \mathcal{J}(C)^\dagger \mathcal{J}(C) = I. \tag{S39}$$

The upper-left block carries transmitted history; the defect blocks carry the complementary history needed for norm preservation. Because $C_{\boldsymbol{r}}$ is built from R_{ts}, this extra channel records a *relative* geometric change rather than a departure from an external identity coframe.

The one-tick source–target history $\widetilde{U}[E, L]$ is the fixed ordered product of the parity-completed recurrence update, spin/frame transport, and the eight port Julia dilations. Port blocks are retained until the occupied response is formed. The scalar transition data used below therefore come directly from this finite ordered history; no unspecified continuum regulator is introduced.

S2.5 Occupied Gaussian state and transition data

Assume that the one-particle history has a gap at the quasienergy cut. The occupied projector is

$$P_- = \chi_{(-\pi,0)}\left(\mathrm{Arg}\,\widetilde{U}\right), \tag{S40}$$

and the many-body reference state is the Gaussian Slater state filling P_-. The normalized closed-time-path influence is

$$e^{i\Gamma_{\mathrm{hist}}[+,-]} = \det\left[(1 - P_-) + P_- \widetilde{U}_-^\dagger \widetilde{U}_+\right]. \tag{S41}$$

Equal histories give one. A first derivative with respect to a geometric source gives the mean occupied source. A second derivative contains both the two-vertex bubble and the direct contact term because both arise from the same nonlinear history. The complete one-particle determinant is not used: unit-determinant elementary gates make it insensitive to the occupied orientation and micromotion needed for response.

For the flat route blocks define

$$\Delta = \sin m, \quad s_{\boldsymbol{r}} = 2\sin\theta_{\boldsymbol{r}}, \quad E_{\boldsymbol{r}} = \sqrt{\Delta^2 + s_{\boldsymbol{r}}^2}, \quad G_{\boldsymbol{r}} = \Delta + E_{\boldsymbol{r}}. \tag{S42}$$

At rest, the four-component recurrence block has two occupied and two empty states. A geometry generator that connects the two sectors therefore has four occupied-to-empty Clifford matrix elements per oriented port. The BCC history has eight oriented ports, so the temporal Kubo coefficient is

$$Z_t = \sum_{\boldsymbol{r}=1}^{8} \sum_{\alpha=1}^{4} \frac{|V_{\boldsymbol{r}\alpha}|^2}{4\Delta} = 8 \times 4\, \frac{g_{\text{port}}^2}{4\Delta}. \tag{S43}$$

The equal-parity normalization is already included in the definition of g_{port}. The spatial relative-cofactor calculation in Sec. S3 gives the one-cell coefficient $z_{\text{cell}}(m)$. Requiring temporal and spatial variations to describe the same tensor coordinate sets $Z_t = z_{\text{cell}}$ and therefore

$$32\frac{g_{\text{port}}^2}{4\Delta} = z_{\text{cell}}, \qquad \boxed{g_{\text{port}}^2 = \frac{\Delta z_{\text{cell}}}{8}.} \tag{S44}$$

The factor 32 is thus the explicit channel count 8 ports times 2 occupied times 2 empty states, not a fitted multiplicity. The transition weights in the exact finite kernel are

$$A_{\boldsymbol{r}} = \frac{g_{\text{port}}^2 \Delta}{2} \frac{G_{\boldsymbol{r}}}{E_{\boldsymbol{r}}}. \tag{S45}$$

Equations (S42), (S43), and (S45) completely specify the displayed one-cell Gaussian response.

S2.6 Relational constraint data

For nonzero incidence $\boldsymbol{\kappa}$, an event-section displacement $\boldsymbol{\xi}$ acts on a symmetric shell by

$$(G_\kappa \xi)_{ij} = i(\kappa_i \xi_j + \kappa_j \xi_i), \tag{S46}$$

and the scalar physical-state functional is

$$Q_\kappa h = (\kappa_i \kappa_j - \kappa^2 \delta_{ij}) h_{ij}. \tag{S47}$$

The identity $Q_\kappa G_\kappa = 0$ makes these maps a complex. The physical tensor space is $\ker Q_\kappa / \operatorname{im} G_\kappa$, which is two dimensional for $\boldsymbol{\kappa} \neq 0$. These are classical reduction maps in the present hybrid theory. Their exact finite path completion is described in Section S6.

S3 Exact hybrid induction of the physical tensor kernel

Throughout this section the occupied route history is quantum, while the centered-Gram strain is a provisional classical source. “Induced” means that the coefficient of the source’s quadratic response is calculated from the occupied history with $Z_{\text{EH}}^{\text{bare}} = 0$; it does not mean that the coframe itself has been quantized or microscopically selected.

S3.1 The two-level occupied line

The geometry-active part of one route reduces to a two-level occupied–empty line. The basis vector $|0\rangle$ may be read as the transmitted component and $|1\rangle$ as its complementary Julia component. Up to a phase convention that drops from the radial metric, the occupied state is

$$|u_-(x)\rangle = \frac{|0\rangle - \sqrt{x}\,|1\rangle}{\sqrt{1+x}}, \qquad x = \cos^2 m\,\cos^2\theta_{\boldsymbol{r}}. \tag{S48}$$

The two probabilities are

$$p_0 = \frac{1}{1+x}, \qquad p_1 = \frac{x}{1+x}. \tag{S49}$$

A logarithmic relative-cofactor strain s changes the ratio of the two amplitudes, $\sqrt{x} \mapsto e^s\sqrt{x}$, without introducing a new state. The Fubini–Study line element measures how distinguishable the strained occupied ray is from the original one:

$$g_{ss}(x) = \langle \partial_s u_- | \partial_s u_- \rangle - |\langle u_- | \partial_s u_- \rangle|^2 = \frac{x}{(1+x)^2}. \tag{S50}$$

The result is positive and vanishes when one component completely dominates. Physically, a route can respond to geometry only when transmitted and complementary histories both participate. This elementary line is the building block of the full Gaussian occupied metric; all additional degeneracy enters through the invariant total oscillator strength $\mathcal{Z}_{\mathrm{occ}}$.

S3.2 One-cell occupied coefficient

For one port define $x_{\boldsymbol{r}} = \cos^2 m \cos^2\theta_{\boldsymbol{r}}$. With equal parity occupation and inversion-related routes counted once, the connected finite occupied metric is

$$C_m(0) - C_m(\boldsymbol{q}), \qquad C_m(\boldsymbol{q}) = \frac{1}{2}\sum_{\boldsymbol{r}\in\mathcal{R}} \frac{x_{\boldsymbol{r}}}{(1+x_{\boldsymbol{r}})^2}. \tag{S51}$$

Its low-momentum expansion is

$$C_m(0) - C_m(\boldsymbol{q}) = z_{\mathrm{cell}}(m) q^2 + O(q^4). \tag{S52}$$

Indeed, with $f(x) = x/(1+x)^2$ and $x_{\boldsymbol{r}} = \cos^2 m[1 - \theta_{\boldsymbol{r}}^2 + O(q^4)]$,

$$f'(\cos^2 m) = \frac{\sin^2 m}{(1+\cos^2 m)^3}, \qquad \frac{1}{2}\sum_{\boldsymbol{r}\in\mathcal{R}} \theta_{\boldsymbol{r}}^2 = q^2, \tag{S53}$$

so

$$\boxed{z_{\mathrm{cell}}(m) = \frac{\cos^2 m\,\sin^2 m}{(1+\cos^2 m)^3} > 0.} \tag{S54}$$

The coefficient vanishes at the open endpoint $m = 0$ and at complete closure $m = \pi/2$; it is positive only when recurrence and inter-event transmission coexist.

Using the transition data in Eq. (S42) and the vertex normalization in Eq. (S44), the exact inverse response on either physical helicity is

$$\boxed{K_{\mathrm{occ}}(\omega, \boldsymbol{q}) = 4\sum_{\boldsymbol{r}\in\mathcal{R}} A_{\boldsymbol{r}} \frac{s_{\boldsymbol{r}}^2 - \nu(\omega)^2}{G_{\boldsymbol{r}}^2 - \nu(\omega)^2},} \qquad \nu(\omega) = 2\sin\frac{\omega}{2}. \tag{S55}$$

No term proportional to a bare Einstein coefficient has been added.

Theorem S3.1 (Hybrid induced massless branch)**.** *In the hybrid model of Definition S2.1, restrict the quantum Gram sector of Proposition S2.2 to its classical Legendre-dual mean field and evaluate the gapped Gaussian occupied route history on that source. Then the kernel in Eq.* (S55) *satisfies, for* $0 < m < \pi/2$*:*

1. $K_{\rm occ}(0,0) = 0$ *without parameter tuning;*

2. *its two-derivative expansion on the physical quotient is*

$$K_{\rm occ} = z_{\rm cell}\,[q^2 - \omega^2] + O(p^4); \tag{S56}$$

3. *the same scalar kernel multiplies the two physical helicities;*

4. *every geometry-visible finite-band residue is positive and the zero-temperature noise is nonnegative.*

The theorem induces the quadratic response of a classical mean field whose coordinate has an explicit quantum-port origin; it does not integrate over that field, quantize its dynamics, or determine its absolute physical scale.

Proof. At $\boldsymbol{q} = 0$, every $s_{\boldsymbol{r}}$ vanishes, so each summand in Eq. (S55) vanishes at $\omega = 0$. For one transition the Euclidean bubble–contact kernel is

$$K_1(\Omega, s) = \frac{g_{\rm port}^2 \Delta}{2} \frac{(\Delta + E_s)(\Omega^2 + s^2)}{E_s[(\Delta + E_s)^2 + \Omega^2]}. \tag{S57}$$

At rest its Ω^2 coefficient is $g_{\rm port}^2/(4\Delta)$. Equation (S43) sums the 8×4 equivalent transitions and Eq. (S44) makes that sum equal to $z_{\rm cell}$. The route-incidence expansion gives the same coefficient multiplying ρ_H, which proves Eq. (S56). Relative-cofactor transport makes the traceless shell Hessian scalar, and projection to the rank-two physical quotient therefore gives the same kernel for both helicities. The Stieltjes decomposition in Sec. S8 proves the residue and noise signs. □

The symbol $z_{\rm cell}(m)$ denotes the one-cell coefficient in Eq. (S54). The symbol $\mathcal{Z}_{\rm occ}$ denotes the invariant sum of such geometry-active occupied transition strengths in any multi-channel realization. In the displayed one-cell model, $\mathcal{Z}_{\rm occ} = z_{\rm cell}(m)$.

The numerical benchmark $m = 0.61$ used in figures and audits is not selected by the theory or by observation. It is an interior test point for which both the open fraction $\cos^2 m \simeq 0.672$ and recurrent fraction $\sin^2 m \simeq 0.328$ are nonzero, the coefficient $z_{\rm cell}$ is well conditioned, and finite-spacing corrections are visible without approaching either endpoint. All analytic theorems hold throughout $0 < m < \pi/2$.

S4 Relational metric, physical quotient, and constrained Fierz–Pauli equivalence

S4.1 Centered-Gram reconstruction

Let four closed port vectors form the columns of a full-rank 3×4 matrix X, so $X\mathbf{1} = 0$. Their Gram matrix

$$\mathcal{G} = X^T X, \qquad \mathcal{G}\mathbf{1} = 0, \tag{S58}$$

is positive semidefinite of rank three. A common $SO(3)$ rotation of X leaves $\mathcal{G}$ unchanged, and conversely two positively oriented full-rank frames with the same Gram matrix differ by one common rotation. The centered Gram cone therefore carries exactly the six components of a positive spatial metric modulo local orientation.

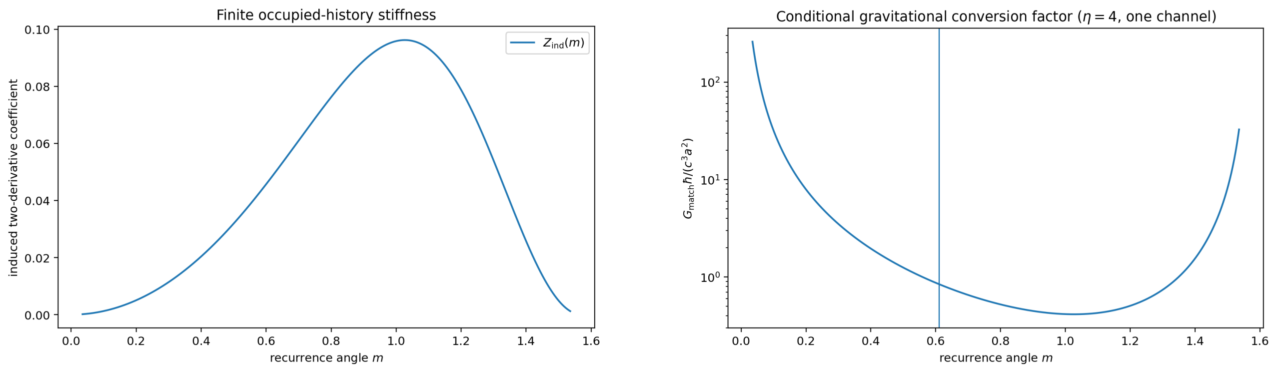

(a) One-cell occupied coefficient $z_{\mathrm{cell}}(m)$.

(b) Conditional conversion $G_{\mathrm{match}}\hbar/(c^3a^2)$ for the primitive coordinate convention.

Figure S1: The occupied response is nonzero only in the interior of the recurrence interval. The vertical line at $m = 0.61$ marks a representative numerical audit point chosen away from both endpoint degeneracies; it is not a dynamically selected or phenomenologically fitted value. Panel (b) is a conversion factor under $\eta = 4$ and one occupied channel, not a prediction of the observed Newton constant.

For the tetrahedral matrix T with $T^T T = (4/3)I$, let the cofactor metric be $C = \det(q)q^{-1}$. The finite register is

$$\mathcal{G} = TCT^T, \tag{S59}$$

and the exact inverse is

$$C = \frac{9}{16}T^T\mathcal{G}T, \qquad q = \sqrt{\det C}\, C^{-1}. \tag{S60}$$

Thus the six local shell directions are reconstructed without an absolute spatial frame. The same four ports and one temporal normal generate ten bivectors whose Parseval frame reconstructs the algebraic Riemann operator once the metric-compatible Cartan connection is supplied. Details are summarized in Section S16.

S4.2 Finite constraint complex

For nonzero spatial incidence $\boldsymbol{\kappa}$, define

$$(G_\kappa \boldsymbol{\xi})_{ij} = \kappa_i\xi_j + \kappa_j\xi_i, \tag{S61}$$

$$Q_\kappa h = (\kappa_i\kappa_j - |\boldsymbol{\kappa}|^2\delta_{ij})h_{ij}. \tag{S62}$$

Then $Q_\kappa G_\kappa = 0$, $\operatorname{rank} G_\kappa = 3$, and $\operatorname{rank} Q_\kappa = 1$. Hence

$$\mathcal{H}^1_\kappa = \frac{\ker Q_\kappa}{\operatorname{im} G_\kappa} \tag{S63}$$

has dimension two. In a frame with $\boldsymbol{\kappa} \parallel \hat{z}$, the survivors are $h_{11} = -h_{22}$ and $h_{12} = h_{21}$.

Let Π_G project onto $\operatorname{im} G_\kappa$, let Π_Q project onto the one-dimensional scalar complement, and set

$$\Pi_H = I - \Pi_G - \Pi_Q, \qquad \operatorname{rank}\Pi_H = 2. \tag{S64}$$

The induced physical kernel is $K_{\mathrm{ind}}\Pi_H$.

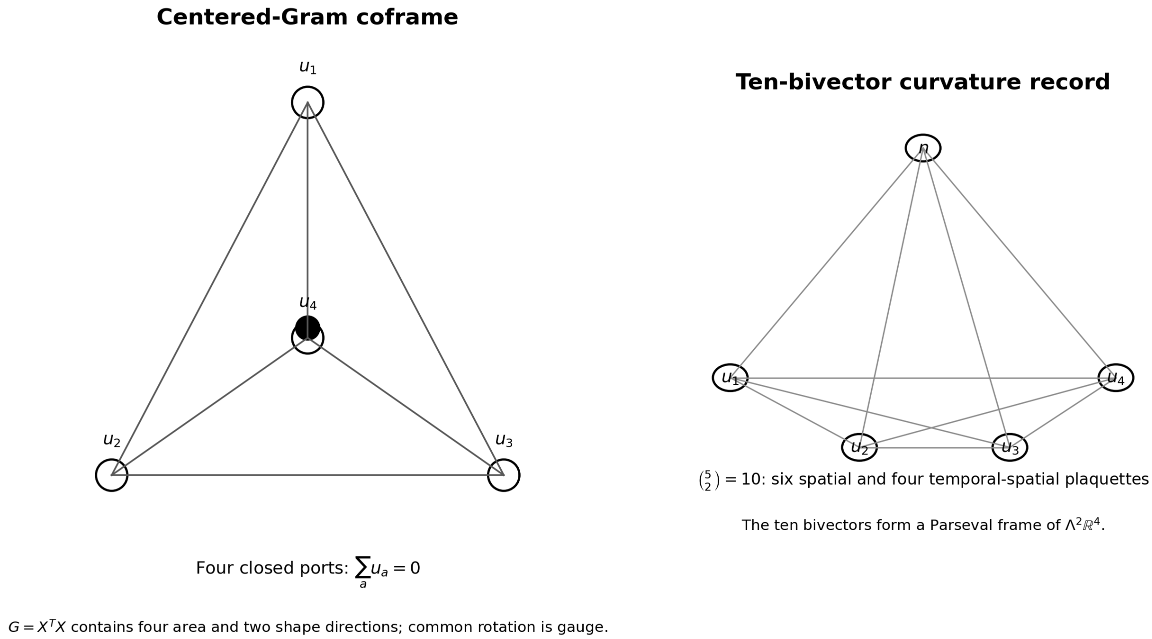

Figure S2: Relational geometry used by the induced theory. Four closed ports reconstruct the complete positive spatial metric; neighboring coframes define transport; ten centered plaquettes reconstruct curvature. The induced result concerns the kinetic coefficient and covariance completion, not merely this kinematic reconstruction.

S4.3 Why a positive induced metric yields Fierz–Pauli after the scalar constraint

The occupied Euclidean metric is positive. The off-shell Fierz–Pauli kinetic form is indefinite in the scalar direction. These facts are not contradictory because the scalar direction is constrained rather than quantized as a physical oscillator.

Let p^2 denote the two-derivative Lorentzian symbol. On a gauge-fixed complement to $\operatorname{im} G_\kappa$, the induced positive representative and Fierz–Pauli representative may be written

$$K_+ = \mathcal{Z}_{\rm occ} p^2 (\Pi_H + 2\Pi_Q), \tag{S65}$$

$$K_{\rm FP} = \mathcal{Z}_{\rm occ} p^2 (\Pi_H - \Pi_Q). \tag{S66}$$

Let q_κ be the symmetric matrix representing the functional Q_κ, so $Q_\kappa h = q_\kappa : h$ and

$$\Pi_Q h = q_\kappa \frac{Q_\kappa h}{\|q_\kappa\|^2}. \tag{S67}$$

Then

$$\frac{1}{2} h : (K_+ - K_{\rm FP}) h = \frac{3\mathcal{Z}_{\rm occ} p^2}{2\|q_\kappa\|^2} (Q_\kappa h)^2. \tag{S68}$$

Theorem S4.1 (Constraint equivalence for the hybrid collective source)**.** *For the provisional classical centered-Gram shell of Definition S2.1, with its coefficient induced by the quantum occupied history, the actions*

$$S_+[h, \lambda] = \frac{1}{2} h : K_+ h + \lambda Q_\kappa h, \tag{S69}$$

$$S_{\rm FP}[h, \lambda'] = \frac{1}{2} h : K_{\rm FP} h + \lambda' Q_\kappa h \tag{S70}$$

are algebraically equivalent under

$$\lambda' = \lambda + \frac{3\mathcal{Z}_{\rm occ}p^2}{2\|q_\kappa\|^2} Q_\kappa h. \tag{S71}$$

They have the same constraint surface, reduced equations, and two-helicity propagator.

Proof. Substitution of (S71) into $S_{\rm FP}$ adds precisely the constraint-square term (S68). Since λ is algebraic, the transformation is invertible and does not change the physical cohomology. Thus the occupied determinant need not generate an indefinite physical norm: its positive response, together with the scalar constraint defined in Sec. S2, yields the same reduced two-helicity equations as the Fierz–Pauli representative. □

No independent Einstein kinetic coefficient is used in this equivalence. The occupied history supplies the positive coefficient, while the displayed scalar constraint supplies the off-shell representative change. This statement remains hybrid: the constraint acts on a provisional classical collective geometry.

S5 Controlled quantum-Gram back-reaction

The mean-field calculation identifies six explicit quantum Gram operators but originally evaluates the occupied history at their expectation value. This section computes the first correction. The result is an exact Gaussian or random-phase calculation in the displayed finite Hilbert space; it is not a full path integral over coframes.

S5.1 Legendre Hessian of the quantum Gram chart

Let $\boldsymbol{g}$ denote the six Gram observables in the ordering of Eq. (S31), and let χ_G be their exact symmetrized covariance in Proposition S2.2. A symmetric strain $h \in \mathrm{Sym}^2(\mathbb{R}^3)$ changes the centered Gram coordinates through the exact tangent map $\delta\mathcal{G}(h) = 2T[(\operatorname{Tr} h)I - h]T^{\mathsf{T}}$. In an orthonormal six-component strain basis,

$$\delta\boldsymbol{g} = B\,\boldsymbol{h}, \qquad H_G = B^{\mathsf{T}}\chi_G^{-1}B, \qquad C_G = H_G^{-1}. \tag{S72}$$

Here H_G is the Legendre Hessian of the quantum Gram saddle and C_G is its Gaussian strain covariance. The exact calibration gives

$$\operatorname{spec}(H_G) = \left(\frac{432}{139}, \frac{432}{139}, \frac{432}{139}, \frac{288}{49}, \frac{288}{49}, \frac{288}{7}\right), \tag{S73}$$

$$\operatorname{spec}(C_G) = \left(\frac{7}{288}, \frac{49}{288}, \frac{49}{288}, \frac{139}{432}, \frac{139}{432}, \frac{139}{432}\right). \tag{S74}$$

Both matrices are positive and rank six. For incidence along a route axis, the two physical tensor eigenvalues of $C_H = U_H^{\mathsf{T}} C_G U_H$ are $49/288$ and $139/432$; on a body diagonal they coincide at $0.2712191358\ldots$.

S5.2 Exact Gaussian integration

Let K_+ denote the positive occupied shell kernel, including its exact frequency dependence when required. Coupling the quantum Gram fluctuation δh to the same relative-cofactor source gives

$$\Gamma^{(2)}[h,\delta h] = \frac{1}{2}\delta h^{\mathsf{T}} H_G \delta h + \frac{1}{2}(h+\delta h)^{\mathsf{T}} K_+ (h+\delta h). \tag{S75}$$

The Gaussian integral over δh is exact and gives

$$\boxed{K_{\rm red} = K_+ - K_+(H_G + K_+)^{-1}K_+.} \tag{S76}$$

This is the matrix parallel sum. On the invertible physical support,

$$\boxed{K_{\rm red}^{-1} = K_+^{-1} + C_G.} \tag{S77}$$

Thus the Gram sector adds an analytic positive covariance to the physical propagator. On a simultaneous eigenchannel, $k_{\rm red} = k/(1 + ck)$ and $D_{\rm red} = 1/k + c$, where $c > 0$ is the corresponding eigenvalue of C_G. At low momentum,

$$K_{H,\rm red} = \mathcal{Z}_{\rm occ}p^2 I_2 - \mathcal{Z}_{\rm occ}^2 p^4 C_H + O(p^6). \tag{S78}$$

The first term is unchanged. The correction cannot generate a mass or alter the common two-derivative cone.

Theorem S5.1 (Gaussian stability of constraint protection)**.** *Assume $H_G \succ 0$, a positive occupied kernel $K_+ \succeq 0$ below the first absorptive threshold, and the event-section/scalar complex of Eqs.* (S61)–(S62)*. Then:*

1. *the corrected Gram susceptibility $(H_G + K_+)^{-1}$ is positive and rank six;*
2. *the physical quotient remains two dimensional for every nondegenerate fluctuating coframe;*
3. *a transverse-tensor drive leaves its incidence direction and physical projector unchanged exactly;*
4. *on the invertible physical support the corrected propagator is $D_{\rm red} = K_+^{-1} + C_G$, so every physical pole and its residue are unchanged and no additional propagator pole is generated;*
5. *a solution of $1 + ck(x_*) = 0$ is a zero of $D_{\rm red} = 1/k + c$ (an antiresonance), not a new excitation.*

Hence the Gaussian correction preserves masslessness, constraint protection and the complete physical spectral measure at this order.

Proof. The first statement follows from $H_G + K_+ \succ 0$. The rank of the complex depends only on nonzero incidence and positive coframe determinant, so smooth Gaussian fluctuations cannot change it before a degeneracy is reached. For a transverse-traceless strain with $h\boldsymbol{n} = 0$, $e^{h/2}\boldsymbol{n} = \boldsymbol{n}$, so the incidence covector and projector are unchanged. The parallel-sum identity (S77) shows that the Gram correction adds the frequency-analytic matrix C_G to the propagator. It therefore creates no pole and does not change the principal part at any existing pole. On a scalar eigenchannel, $1 + ck = 0$ makes $K_{\rm red}$ singular but $D_{\rm red}$ zero, proving the final statement. □

At $m = 0.61$, the norm controlling the expansion,

$$\epsilon_G(q) = \left\| C_G^{1/2} K_+(q) C_G^{1/2} \right\|_2, \tag{S79}$$

is 3.80×10^{-5} at $q = 0.05$, 1.52×10^{-4} at $q = 0.1$, and 1.52×10^{-2} at $q = 1$. The corrected susceptibility remains positive and rank six at every tested value. One thousand Gaussian coframes at each width $\sigma = 0.01, 0.03, 0.05, 0.10$ retained an orthogonal rank-two projector, for 4,000 samples in total. For the generic $q = 0.1$ audit, the two physical Gram eigenchannels produce propagator zeros at 98.84% and 99.52% of the interval from the low pole to the first pair threshold. The parallel-sum identity is satisfied to 5.68×10^{-14}, the original pole and residue are unchanged, and no additional physical pole is present.

The feedback can introduce zeros of the corrected propagator close to a pair threshold, but it adds no physical pole. The one-pole conservative spectrum, noise-quiet interval and original massless branch therefore survive at Gaussian order. The non-Gaussian correction, dynamical quantum constraint algebra and full coframe measure remain open.

Table S2: Controlled quantum-Gram correction at the representative interior point $m = 0.61$.

q	$\mathcal{Z}_{\mathrm{occ}} q^2$	$\epsilon_G(q)$	$\mathrm{rank}(H_G + K_+)^{-1}$
0.05	1.18×10^{-4}	3.80×10^{-5}	6
0.10	4.72×10^{-4}	1.52×10^{-4}	6
0.30	4.25×10^{-3}	1.37×10^{-3}	6
0.50	1.18×10^{-2}	3.80×10^{-3}	6
0.80	3.02×10^{-2}	9.72×10^{-3}	6
1.00	4.72×10^{-2}	1.52×10^{-2}	6

S6 Exact path-valued covariance and continuum completion

S6.1 Exact finite algebra

A nonzero translation-invariant derivative on a finite periodic set cannot satisfy the ordinary sitewise Leibniz rule: its Fourier symbol would obey $\delta(k + \ell) = \delta(k) + \delta(\ell)$ on a finite group, forcing $\delta = 0$. The exact derivative is instead the graph coboundary

$$(df)_e = f_t - f_s, \tag{S80}$$

which maps sites to oriented edges and obeys an endpoint-cup product rule.

For a graph with V vertices, let

$$Q(A, B, L) = \frac{1}{2}\pi^T A\pi + \pi^T L\phi + \frac{1}{2}\phi^T B\phi, \tag{S81}$$

with $A = A^T$ and $B = B^T$. Associate

$$X(A, B, L) = \begin{pmatrix} L & A \\ -B & -L^T \end{pmatrix} \in \mathfrak{sp}(2V, \mathbb{R}). \tag{S82}$$

Then

$$\{Q_X, Q_Y\} = Q_{[X,Y]}, \tag{S83}$$

so the finite algebra is exactly Jacobi closed. Nearest-link generators are not closed; commutators generate longer paths. Matrix support supplies a natural path-length filtration.

For recurrence-normalized normals

$$H_{\mathcal{Z}_{\mathrm{occ}}}[N] = \frac{1}{2\mathcal{Z}_{\mathrm{occ}}}\pi^T \operatorname{diag}(N)\pi + \frac{\mathcal{Z}_{\mathrm{occ}}}{2}\phi^T K_N \phi, \tag{S84}$$

the coefficient $\mathcal{Z}_{\mathrm{occ}}$ cancels from the normal–normal bracket. Likewise, a gapped fermion Hamiltonian $h_\Delta = K + \Delta\Gamma$, with $\{K, \Gamma\} = 0$, obeys

$$[A_\Delta[N], A_\Delta[M]] = \frac{1}{4}[\{D_N, K\}, \{D_M, K\}], \tag{S85}$$

so the rest gap does not deform the current algebra.

S6.2 Controlled hypersurface-deformation contraction

For lapse fields N and M, the exact oriented edge cochain is

$$\beta_{\boldsymbol{r}}(x; N, M) = N(x)M(x + a\boldsymbol{r}) - M(x)N(x + a\boldsymbol{r}). \tag{S86}$$

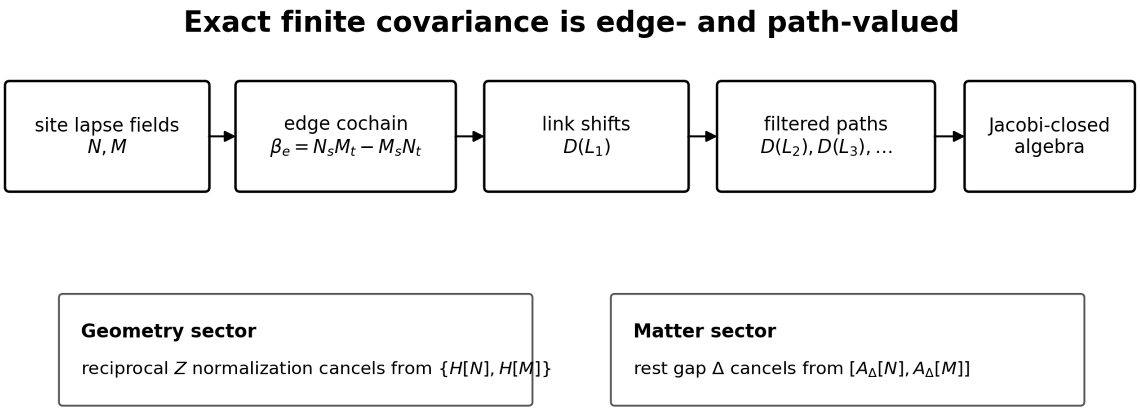

Figure S3: Finite covariance is exact on edges and paths rather than on a nonexistent sitewise derivative. The induced normalization sets physical scales but cancels from the deformation algebra.

For smooth fields,

$$\beta_{\boldsymbol{r}} = a r^i (N \partial_i M - M \partial_i N) + O(a^2). \tag{S87}$$

Let the positive second moment of the route set be

$$M^{ij} = \sum_{\boldsymbol{r}} w_{\boldsymbol{r}} r^i r^j. \tag{S88}$$

The centered-Gram coframe converts M^{ij} to the local inverse metric. Summing the path current yields

$$\{H[N], H[M]\} = D\Big[q^{ij}(N \partial_j M - M \partial_j N)\Big] + O(a^2), \tag{S89}$$

with the standard scalar–shift and shift–shift brackets at the same order. The result is a controlled contraction of the exact path algebra, not an assertion that the finite algebra equals the continuum Dirac algebra at nonzero spacing.

S6.3 Einstein completion at two derivatives

We now state explicitly the assumptions needed to pass from the induced linear sector to nonlinear continuum dynamics.

Assumption S6.1 (Two-derivative completion hypotheses)**.** In the long-wavelength spin-saturated branch:

1. the spatial metric q_{ij} and its conjugate momentum are the only long-range canonical geometric variables;
2. the momentum constraint generates spatial diffeomorphisms;
3. the scalar and momentum constraints represent the hypersurface-deformation algebra with structure function q^{ij} through the leading two-derivative order;
4. the scalar constraint is local, time-reversal invariant, at most quadratic in momenta, and contains no additional long-range scalar;
5. matter couples universally to the same coframe and conserved source.

Within the restricted class defined by Assumption S6.1, the HKT result identifies an ADM representative up to normalization and a cosmological term [6]. Within the corresponding local universal-coupling class, the Deser construction identifies an Einstein representative for the nonlinear completion of Fierz–Pauli theory [4]. These are conditional equivalence statements: relaxing locality, field content, derivative order, algebra, or universal coupling permits inequivalent theories. The microscopic calculation fixes the quadratic normalization inside this restricted class.

Corollary S6.2 (Restricted Einstein representative of the hybrid model)**.** *For the hybrid model of Definition S2.1, and only under Assumption S6.1, the leading local two-derivative continuum theory is equivalent within the stated restricted class to the representative*

$$\Gamma_{\text{eff}}[g] = \frac{c^3}{16\pi G_{\text{match}}} \int \mathrm{d}^4x \sqrt{-g}\,(R - 2\Lambda_{\text{glob}}) + a^2\Gamma_4[g] + O(a^4\partial^6), \tag{S90}$$

where G_{match} is the conversion normalization in Sec. S7. The normalized relative influence does not determine the global common-history phase Λ_{glob}, and the displayed action is one representative modulo the ambiguities in Sec. S6.4.

The corollary is an equivalence statement inside the restricted two-derivative class, not a direct equality between the microscopic determinant and $\int \sqrt{-g}R$ at every frequency. The exact finite kernel remains the calculated response; Eq. (S90) is a conditional local representative. The Newtonian Poisson equation used below is inherited from this representative and is not independently derived from a microscopic static source.

S6.4 Residual ambiguity of the continuum uniqueness step

The HKT, Lovelock, Weinberg, and Deser results are restrictive but not assumption-free uniqueness theorems. In the present application they leave the following residual ambiguity.

1. **Choice of canonical representative.** Local canonical transformations, lapse densitizations, and invertible field redefinitions can change the off-shell appearance of the constraints while preserving the same reduced two-derivative physics. Our claim is equivalence to an Einstein representative, not literal equality of every microscopic variable with the ADM metric.

2. **Terms invisible to the local equations used here.** A cosmological constant, boundary completions, and four-dimensional topological densities are not fixed by the local tensor kernel. In a first-order extension, Holst, Nieh–Yan, and torsion-squared terms can also remain unless their microscopic coefficients are computed.

3. **Higher derivatives and preferred-frame operators.** The uniqueness arguments do not remove the $a^2\Gamma_4$ sector. Curvature-squared operators, order-reduced higher-time-derivative terms, and cubic-route Lorentz-violating operators may be shifted among one another by local field redefinitions, but their on-shell dispersion and source corrections remain physical.

4. **Relaxed assumptions.** Nonlocality, additional long-range fields, a deformed algebra of hypersurface deformations, higher powers of canonical momenta, or a preferred foliation permit inequivalent continuum theories. The finite path algebra is exact, but only its leading contraction has been shown to take the undeformed HKT form.

5. **Quantum completion.** These theorems do not select a path-integral measure, operator ordering, global topology, quantum state, or anomaly-free quantum constraint representation.

Accordingly, "Einstein representative" below always means equivalence within the local spin-saturated two-derivative class defined by Assumption S6.1. It does not mean that the microscopic variables are uniquely the ADM variables, that all finite-spacing completions are Einsteinian, or that a quantum completion has been selected.

S7 Effective gravitational normalization and the static continuum representative

S7.1 Continuum normalization

On the two physical helicities, the induced finite action may be written

$$\frac{S_{\mathrm{ind}}^{(2)}}{\hbar} = \frac{\mathcal{Z}_{\mathrm{occ}}}{2} \sum_{n,v} \left[|h_{n+1,v} - h_{n,v}|^2 - \frac{1}{8} \sum_{\boldsymbol{r}\in\mathcal{R}} |h_{n,v+\boldsymbol{r}} - h_{n,v}|^2 \right], \tag{S91}$$

where $\mathcal{Z}_{\mathrm{occ}}$ is the total occupied oscillator strength. For one displayed channel, $\mathcal{Z}_{\mathrm{occ}} = z_{\mathrm{cell}}(m)$; for a filled internal sea, the channel contributions add.

Let $t = n\tau$, $x^i = av^i$, $c = a/\tau$, and let v_0 be the physical volume per event in the flat vacuum. Then

$$\sum_{n,v} \longrightarrow \frac{1}{\tau v_0} \int \mathrm{d}t\, \mathrm{d}^3x. \tag{S92}$$

The route moment identity $(1/8)\sum r_i r_j = \delta_{ij}$ gives

$$S_{\mathrm{ind}}^{(2)} \longrightarrow \frac{\hbar \mathcal{Z}_{\mathrm{occ}} a^2}{2\tau v_0} \int \mathrm{d}t\, \mathrm{d}^3x \left[\frac{1}{c^2} |\dot{h}|^2 - |\nabla h|^2 \right]. \tag{S93}$$

In the orthonormal two-helicity convention, the Einstein transverse-traceless action is

$$S_{\mathrm{EH}}^{\mathrm{TT}} = \frac{c^4}{64\pi G} \int \mathrm{d}t\, \mathrm{d}^3x \left[\frac{1}{c^2} |\dot{h}|^2 - |\nabla h|^2 \right]. \tag{S94}$$

Equating the two prefactors gives

$$\frac{\hbar \mathcal{Z}_{\mathrm{occ}} a^2}{2\tau v_0} = \frac{c^4}{64\pi G}. \tag{S95}$$

Using $\tau = a/c$ produces

$$\boxed{G_{\mathrm{match}} = \frac{c^3 v_0}{32\pi \hbar a \mathcal{Z}_{\mathrm{occ}}}.} \tag{S96}$$

The factor 32 is therefore 64/2: 64π is the standard orthonormal transverse-traceless Einstein normalization, while the discrete action carries the conventional factor 1/2. It is independent of the separate microscopic 8×4 channel count in Eq. (S43); the two appearances of 32 have different origins. The two origins can be compared without suppressing either count:

$$8 \times 2 \times 2 = 32, \qquad \text{routes} \times \text{occupied states} \times \text{empty states}, \tag{S97}$$

$$64/2 = 32, \qquad \text{TT Einstein denominator / discrete quadratic prefactor.} \tag{S98}$$

The equality of the integers is not itself a physical identity; the first fixes the one-cell vertex normalization, whereas the second converts the already summed tensor stiffness into the conventional continuum coefficient.

S7.2 Event-volume normalization and the primitive BCC convention

The continuum match depends on the physical volume represented by one collective event. Write

$$v_0 = \eta a^3, \tag{S99}$$

where η is dimensionless. The graph fixes a primitive coordinate volume but does not by itself prove that the coframe normalization assigning physical length a to one route is nature's normalization.

One connected BCC component is generated by

$$\boldsymbol{r}_1 = (1,1,1), \quad \boldsymbol{r}_2 = (1,-1,-1), \quad \boldsymbol{r}_3 = (-1,1,-1). \tag{S100}$$

Their determinant has magnitude four. Thus the *primitive coordinate convention* used in the explicit audit has

$$\eta_{\mathrm{BCC}} = 4, \qquad v_0 = 4a^3. \tag{S101}$$

For general η, the one-channel spectral relation is

$$\boxed{G_{\mathrm{match}}(m,a;\eta) = \frac{\eta c^3 a^2}{32\pi\hbar z_{\mathrm{cell}}(m)}.} \tag{S102}$$

In the primitive convention, this reduces to

$$\boxed{G_{\mathrm{match}}(m,a) = \frac{c^3a^2}{8\pi\hbar z_{\mathrm{cell}}(m)} = \frac{c^3a^2}{8\pi\hbar}\frac{(1+\cos^2 m)^3}{\cos^2 m\sin^2 m}.} \tag{S103}$$

Equivalently,

$$\ell_{P,\mathrm{match}}^2 = \frac{\eta a^2}{32\pi z_{\mathrm{cell}}(m)}, \tag{S104}$$

and the familiar $a^2/(8\pi z_{\mathrm{cell}})$ follows only for $\eta = 4$. For the representative audit point $m = 0.61$, the primitive coordinate convention $\eta = 4$, and one occupied channel,

$$z_{\mathrm{cell}} = 0.0471837339, \qquad \frac{G_{\mathrm{match}}\hbar}{c^3a^2} = 0.843272299, \qquad \frac{a}{\ell_{P,\mathrm{match}}} = 1.08897042. \tag{S105}$$

These numbers only translate between a and the conditional continuum normalization after choosing m, η, and the one-channel occupation. They are not predictions of the observed G, a, η, or the physical coframe normalization.

S7.3 Direct finite static branch and source rigidity

The static response can be obtained from the finite constraints without invoking the HKT/Deser nonlinear uniqueness step. Write the linear canonical maps as

$$\dot h = \mathcal{Z}_{\mathrm{occ}}^{-1}\mathsf{M}p + G_{\boldsymbol{\kappa}}\boldsymbol{\beta}, \qquad \dot p = -\mathcal{Z}_{\mathrm{occ}}\mathsf{K}_{\boldsymbol{\kappa}}h - \Theta, \tag{S106}$$

with the finite identities

$$Q_{\boldsymbol{\kappa}}G_{\boldsymbol{\kappa}} = 0, \qquad G_{\boldsymbol{\kappa}}^{\mathsf{T}}\mathsf{K}_{\boldsymbol{\kappa}} = 0, \tag{S107}$$

$$Q_{\boldsymbol{\kappa}}\mathsf{M} = \frac{1}{2}\boldsymbol{\kappa}^{\mathsf{T}}G_{\boldsymbol{\kappa}}^{\mathsf{T}}, \qquad \frac{1}{2}G_{\boldsymbol{\kappa}}^{\mathsf{T}}\Theta = \Theta\boldsymbol{\kappa}. \tag{S108}$$

Allow initially independent scalar and momentum normalizations,

$$\mathcal{C}_0 = a_0 Q_{\boldsymbol{\kappa}}h - \varepsilon, \qquad \boldsymbol{\mathcal{C}} = b_0 G_{\boldsymbol{\kappa}}^{\mathsf{T}}p - \boldsymbol{j}, \tag{S109}$$

for sources satisfying $\dot\varepsilon = \boldsymbol{\kappa}\cdot\boldsymbol{j}$ and $\dot{\boldsymbol{j}} = -\Theta\boldsymbol{\kappa}$.

Theorem S7.1 (Source-normalization rigidity). *The constraints in Eq. (S109) propagate for every locally conserved source if and only if*

$$\boxed{a_0 = \mathcal{Z}_{\mathrm{occ}}, \qquad b_0 = \frac{1}{2}.} \tag{S110}$$

Thus the physical tensor response, scalar source and momentum source cannot be assigned independent dimensionless gravitational normalizations.

Proof. Differentiating Eq. (S109) with Eqs. (S106)–(S108) gives

$$\dot{\mathcal{C}}_0 = \frac{a_0}{2b_0\mathcal{Z}_{\mathrm{occ}}}\boldsymbol{\kappa}\cdot\boldsymbol{\mathcal{C}} + \left(\frac{a_0}{2b_0\mathcal{Z}_{\mathrm{occ}}} - 1\right)\boldsymbol{\kappa}\cdot\boldsymbol{j}, \tag{S111}$$

$$\dot{\boldsymbol{\mathcal{C}}} = -(2b_0 - 1)\Theta\boldsymbol{\kappa}. \tag{S112}$$

The source-contamination terms vanish for arbitrary $\boldsymbol{j}$ and Θ exactly for Eq. (S110). $\square$

On one connected BCC component define

$$(L_{\mathrm{BCC}}f)_v = 2f_v - \frac{1}{4}\sum_{\boldsymbol{r}\in\mathcal{R}_8} f_{v+\boldsymbol{r}}, \qquad \lambda(\boldsymbol{q}) = 2[1 - \cos q_x \cos q_y \cos q_z]. \tag{S113}$$

The source component has four coherent quadratic valleys. Along an even axis separation,

$$G_{\mathrm{BCC}}(r,0,0) = \frac{1}{\pi^2}\int_0^{\pi} \cos(rx)\, K(\cos^2 x)\,\mathrm{d}x, \tag{S114}$$

where K is the complete elliptic integral. Steepest-valley expansion, or direct evaluation of Eq. (S114), gives

$$\boxed{G_{\mathrm{BCC}}(r) = \frac{1}{\pi r} + O(r^{-3}).} \tag{S115}$$

The numerical fit over $10 \le r \le 100$ gives 0.31830985195 for the asymptotic coefficient, compared with $1/\pi = 0.31830988618$, a relative difference 1.08×10^{-7}.

In the time-symmetric conformal branch $q_{ij} = \phi^4\delta_{ij}$, the sourced finite constraint is

$$\boxed{8\mathcal{Z}_{\mathrm{occ}}\,\phi L_{\mathrm{BCC}}\phi = \varepsilon.} \tag{S116}$$

For a cell-integrated nonnegative source ε_v and positive Dirichlet boundary data it is the stationary equation of

$$\mathcal{J}[u] = 4\mathcal{Z}_{\mathrm{occ}}\langle u, L_D u\rangle - \sum_v \varepsilon_v \log(1+u_v), \qquad \phi = 1 + u, \tag{S117}$$

whose Hessian is strictly positive. The solution is unique and has

$$\boxed{\phi(r) = 1 + \frac{\mathcal{E}_{\mathrm{eff}}}{8\pi\mathcal{Z}_{\mathrm{occ}} r} + O(r^{-3}), \qquad \mathcal{E}_{\mathrm{eff}} = \sum_v \frac{\varepsilon_v}{\phi_v}.} \tag{S118}$$

This is an independent microscopic mean-field static branch using the same coefficient as the tensor response. Identifying the cell-normalized ε with realistic matter density remains a matter-sector dictionary, not an extra gravitational coupling.

For comparison, imposing the restricted continuum Einstein representative converts Eq. (S118) into the conventional Poisson normalization after the matter dictionary and event-volume conversion are chosen. The existence and coefficient sharing of the finite inverse-distance branch do not depend on that step.

bcc_static_green.png

(a) $rG_{\mathrm{BCC}}(r)$ approaches $1/\pi$.

bcc_static_remainder.png

(b) The leading correction scales as r^{-2} in rG.

Figure S4: Direct BCC static response. The inverse-distance coefficient is obtained from the finite scalar operator rather than inherited from continuum uniqueness.

S7.4 Scale-free cross-sector sum rules

The first occupied pair threshold at zero momentum is

$$\Omega_{\mathrm{pair}} = \frac{2mc}{a}. \tag{S119}$$

Eliminating a between (S102) and (S119) gives

$$\boxed{\frac{\hbar G_{\mathrm{match}} \Omega_{\mathrm{pair}}^2}{c^5} = \frac{\eta m^2}{8\pi z_{\mathrm{cell}}(m)}}. \tag{S120}$$

The primitive BCC convention $\eta = 4$ gives $m^2/(2\pi z_{\mathrm{cell}})$. The relation is scale free but not event-normalization free: gravity and the first threshold cannot be adjusted independently once the physical coframe normalization η is fixed.

S8 Exact finite band and controlled effective theory

S8.1 Stieltjes positivity without a bare Einstein term

Grouping equal pair thresholds in (S55) gives

$$K(x) = a_0 - \sum_{\alpha} \frac{\beta_\alpha}{\lambda_\alpha - x}, \qquad \beta_\alpha > 0, \tag{S121}$$

where

$$\beta_\alpha = \sum_{\boldsymbol{r}: G_{\boldsymbol{r}}^2 = \lambda_\alpha} 4A_{\boldsymbol{r}}(G_{\boldsymbol{r}}^2 - s_{\boldsymbol{r}}^2) > 0. \tag{S122}$$

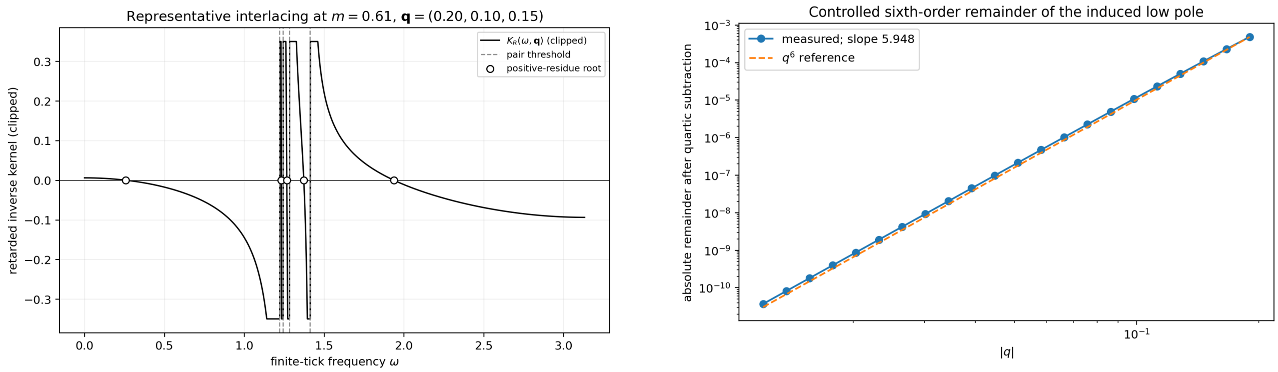

(a) Exact interlacing of thresholds and roots.

(b) Sixth-order remainder after subtracting the induced quartic pole.

Figure S5: The exact finite response, rather than a truncated higher-derivative polynomial, determines the particle content. The audit uses no bare Einstein coefficient and finds a fitted remainder power 5.948.

Hence

$$K'(x) = -\sum_{\alpha} \frac{\beta_\alpha}{(\lambda_\alpha - x)^2} < 0. \tag{S123}$$

There is exactly one low root below the first threshold and at most one root between successive thresholds. Every root is simple. For a principal-band positive-frequency root, the physical residue is positive because the frequency Jacobian is positive while $K'(x) < 0$.

The zero-temperature noise is

$$N(\omega, \boldsymbol{q}) = 4\pi \sum_{r: G_r < 2} \frac{A_r \Delta}{c_r} \left[\delta(\omega - \omega_r) + \delta(\omega + \omega_r)\right] \Pi_H, \tag{S124}$$

with positive line weights. At $\boldsymbol{q} = 0$,

$$|\omega| < \min(2m, \pi/2) \tag{S125}$$

is a quiet interval with no pair production, dissipation, or noise.

S8.2 Induced effective expansion

Because the entire two-derivative coefficient is induced, the horizontal fraction is one. The exact low-frequency expansion is

$$\frac{K_{\text{ind}}}{z_{\text{cell}}} = q^2 - \omega^2 + \frac{\omega^4 - I_4}{12} + \frac{1}{\Delta^2}\left(\omega^2 q^2 - \frac{\omega^4}{4} - \frac{3I_4}{4}\right) + O(p^6). \tag{S126}$$

The low root is

$$\omega_g^2 = q^2 - \Gamma_{\text{ind}}(m) \sum_{i<j} q_i^2 q_j^2 + O(q^6), \qquad \boxed{\Gamma_{\text{ind}}(m) = \frac{1}{3} + \frac{3}{\sin^2 m}.} \tag{S127}$$

The same polynomial multiplies both helicities. In physical units,

$$\Omega_{g,\lambda}^2 = c^2 k^2 - c^2 a^2 \Gamma_{\text{ind}} \mathcal{A}_4(\widehat{\boldsymbol{k}}) k^4 + O(c^2 a^4 k^6), \qquad \lambda = R, L, \tag{S128}$$

Table S3: Exact low-pole error after subtracting the quartic dispersion at the representative benchmark $m = 0.61$. The value is chosen only as a well-conditioned interior audit point, not as a physical prediction. The maximum is over 1024 directions and quantifies the regime in which the $O(q^6)$ statement is numerically controlled.

$\lvert q\rvert = \lvert ak\rvert$	Max. quartic shift in ω^2/q^2	Max. $\lvert R_6\rvert/q^2$
0.025	1.973×10^{-3}	7.18×10^{-6}
0.050	7.893×10^{-3}	1.14×10^{-4}
0.100	3.157×10^{-2}	1.74×10^{-3}

where

$$\mathcal{A}_4 = n_x^2 n_y^2 + n_x^2 n_z^2 + n_y^2 n_z^2 = \frac{1}{2}\left(1 - \sum_i n_i^4\right). \tag{S129}$$

It obeys

$$0 \leq \mathcal{A}_4 \leq \frac{1}{3}, \qquad \langle \mathcal{A}_4 \rangle_{S^2} = \frac{1}{5}, \tag{S130}$$

with zero on a routing axis, 1/4 on a face diagonal, and 1/3 on a body diagonal. The phase and group velocities are

$$\frac{v_{\mathrm{ph}}}{c} = 1 - \frac{1}{2}\Gamma_{\mathrm{ind}}\mathcal{A}_4 (ak)^2 + O((ak)^4), \tag{S131}$$

$$\frac{v_{\mathrm{gr}}}{c} = 1 - \frac{3}{2}\Gamma_{\mathrm{ind}}\mathcal{A}_4 (ak)^2 + O((ak)^4). \tag{S132}$$

Consequently,

$$0 \leq 1 - \frac{v_{\mathrm{gr}}}{c} \leq \frac{1}{2}\Gamma_{\mathrm{ind}}(ak)^2 + O((ak)^4). \tag{S133}$$

This is an explicitly preferred-frame, nonbirefringent anisotropic correction of the same frequency order as mass-dimension-six terms in gravitational Lorentz-violation effective theories [26, 27]. The comparison concerns the propagation shape, not an identification of all SME coefficients. The equal-parity BCC kernel remains proportional to the identity on the two helicities, so the displayed correction produces no velocity birefringence.

For a propagation distance D, the leading phase is

$$\delta\Psi_R = \delta\Psi_L = 4\pi^3 \Gamma_{\mathrm{ind}}\mathcal{A}_4 \frac{Da^2}{c^3} f^3 + O(f^5). \tag{S134}$$

The differentiating conjunction is subluminal sign, f^3 scaling, a cubic sky harmonic, and no helicity splitting.

Size of the controlled remainder. Define the on-shell residual after the quartic term by

$$R_6(\boldsymbol{q}; m) = \omega_{\mathrm{exact}}^2 - \left[q^2 - \Gamma_{\mathrm{ind}}(m)\mathcal{A}_4(\widehat{\boldsymbol{q}})q^4\right]. \tag{S135}$$

At the representative interior benchmark $m = 0.61$ described after Theorem S3.1, the exact-kernel audit fits $R_6 = C_6(\widehat{\boldsymbol{q}})q^6 + O(q^8)$. The fitted coefficients are approximately 0 on an axis, 5.598 on a face diagonal, 18.463 on a body diagonal, and 12.470 for the generic direction used in Figure S5. A 1024-direction Fibonacci-sphere scan gives $0.016 \leq C_6 \leq 18.451$ away from the numerically singular axis fit. Direct errors relative to the leading q^2 term are reported in Table S3.

At the audit point, (S133) becomes $1 - v_{\rm gr}/c \lesssim 4.737(ak)^2$ at quartic order. A programmable simulator can probe $q \sim 0.05$–0.1, where the quartic effect is visible and the exact remainder remains quantified. No astrophysical magnitude is quoted because the physical event scale has not been selected.

The off-shell ω^4 terms in (S126) must be treated perturbatively by order reduction or local field redefinition. They are not additional exact particles: pole counting is performed on (S55). The finite update still selects a microscopic time slicing and route frame. A covariant transformation law between boosted microscopic frames, emission corrections at the source, scattering from frame domains, and the fate of the anisotropy when the route orientation varies cosmologically have not been derived. For isotropically oriented domains the exact angular moments are

$$\langle \mathcal{A}_4 \rangle = \frac{1}{5}, \qquad \left\langle \mathcal{A}_4^2 \right\rangle = \frac{1}{21}, \qquad \mathrm{Var}(\mathcal{A}_4) = \frac{4}{525}. \tag{S136}$$

Thus N independent equal-length domains leave the positive isotropic mean $1/5$ but suppress the rms angular contrast to $\sqrt{4/(525N)}$. This is only a kinematic random-domain estimate. Correlated domains, boundary scattering, cosmological alignment, and the dynamics selecting the microscopic route frame are not derived.

Eliminating a between the dispersion length $L_g = a\sqrt{\Gamma_{\rm ind}}$ and the pair threshold gives

$$\boxed{\frac{\Omega_{\rm pair} L_g}{c} = 2m\sqrt{\Gamma_{\rm ind}(m)}.} \tag{S137}$$

The dispersion amplitude and threshold location therefore form one correlated prediction rather than two independent effective parameters.

S8.3 Finite-kernel matching invariants

The quartic dispersion and sum rules above are consequences of the exact physical two-point function, not of the conditional nonlinear Einstein representative.

Theorem S8.1 (Analytic matching invariance)**.** *Let $D_{\rm loc}^{-1}(\omega, \boldsymbol{q})$ be any local analytic continuum inverse propagator on the two-dimensional physical quotient. If its low pole matches the exact finite root of Eq. (S55) through $O(q^4)$ and its first absorptive threshold matches the same recurrence gap, then it necessarily reproduces*

$$\omega_g^2 = q^2 - \Gamma_{\rm ind}(m)\mathcal{A}_4(\widehat{\boldsymbol{q}})q^4 + O(q^6) \tag{S138}$$

and Eq. (S137). If its tensor coefficient is normalized by the direct source branch of Sec. S7.3, it also obeys Eq. (S120). These statements do not assume HKT/Deser uniqueness.

Proof. Analytic equality of the low root through fourth order fixes the Taylor coefficient uniquely, including its cubic angular harmonic. The pair threshold is the exact branch point $2m$ in tick units, so eliminating the common event length gives Eq. (S137). Source-normalization rigidity and the direct static conversion then give the second sum rule. None of these steps selects nonlinear vertices away from the two-point and static sectors. □

The Gaussian feedback in Eq. (S76) leaves every original zero of the exact inverse kernel unchanged. More strongly, Eq. (S77) shows that it adds only an analytic covariance to the propagator, so the low-pole dispersion, helicity degeneracy and residues are unchanged and no Gram-hybrid excitation is added at this order. The near-threshold antiresonances are propagator zeros. The BCC harmonic itself is representative dependent; the principle that the exact finite kernel fixes the continuum Taylor coefficients is not.

S9 Robustness beyond the exact BCC representative

The BCC choice fixes the exact finite band and its quartic angular fingerprint. The leading closure properties are less specific.

S9.1 Universal structural neighborhood

Theorems S1.1 and S1.2 hold throughout the open set where the complex ranks, positive chart and physical response retain their stated ranks and signs. The randomized ensemble of Table S1 probes conditioning over ten decades, while the deliberate-defect family locates how protection is lost when $QG = 0$ is violated. The recurrence response itself remains above 10% of its maximum for

$$0.27595 < m < 1.47055, \tag{S139}$$

and reaches $z_{\text{cell}}^{\max} = 0.0962250$ at $m = 1.02671$. Thus the positive response is not confined to a finely tuned recurrence angle.

S9.2 Four-port realization neighborhood

Definition S9.1 (Admissible four-port deformation)**.** An admissible route frame consists of four vectors $t_a \in \mathbb{R}^3$ satisfying $\sum_a t_a = 0$ and $\operatorname{rank}(t_1, t_2, t_3, t_4) = 3$, together with their inversion partners and a nonzero occupied gap. Its second moment is $M = (1/4)\sum_a t_a t_a^T \succ 0$.

Theorem S9.2 (Open-neighborhood stability of the hybrid response)**.** *For the hybrid source construction of Definition S2.1, every admissible classical four-port deformation with a nonzero quantum occupied gap has:*

1. *the centered-Gram tangent has rank six;*
2. *after local whitening by $M^{-1/2}$, the two-derivative route moment is isotropic;*
3. *for every nonzero incidence, the event-section/scalar complex has cohomology dimension two;*
4. *every gapped Gaussian occupied kernel with positive transition weights remains Stieltjes, with positive residues and nonnegative noise;*
5. *these properties persist under sufficiently small perturbations until the frame rank or occupied gap closes.*

Proof. Full-rank centered four-port frames form an open subset. The Gram tangent is an isomorphism from $\mathrm{Sym}^2(\mathbb{R}^3)$ to the centered six-dimensional Gram space; its determinant can vanish only at frame degeneracy. Since $M \succ 0$, whitening exists and gives $(1/4)\sum_a (M^{-1/2}t_a)(M^{-1/2}t_a)^T = I$. The rank computation of (S61)–(S62) depends only on $\boldsymbol{\kappa} \neq 0$, not on BCC details. Finally, positive transition weights and a nonzero gap are open conditions, and the Stieltjes derivative is strictly negative between thresholds. □

The accompanying audit perturbed the four closed routes, recentered and whitened them, and tested 200 random frames at each of six perturbation amplitudes. All 1200 samples retained rank six, cohomology dimension two, positive transition weights, positive low-pole residues, and machine-precision moment/constraint identities.

This theorem does not establish robustness to arbitrary non-Gaussian occupation, topology change, or capacity-changing dynamics. It addresses the most direct fine-tuning concern: the closure is not destroyed by perturbing the nondegenerate four-port frame or positive transition data.

Table S4: Which conclusions are stable in an open four-port neighborhood and which remain specific to the BCC representative.

Structure	**Stable under admissible four-port deformations**	**BCC-specific or still open**
Relational geometry	Rank-six centered-Gram tangent and positive local whitening.	Exact route coordinates and primitive-volume convention.
Physical modes	Rank-two event-section/scalar cohomology for nonzero incidence.	Global topology and capacity-changing defects.
Spectral health	Stieltjes interlacing, positive residues, and nonnegative noise while the gap stays open.	Exact threshold locations, mirror sectors, and finite-band trigonometric form.
Lorentz recovery	Common quadratic cone after local whitening.	Cubic harmonic $\mathcal{A}_4$, its coefficient, route-frame domains, and cosmological orientation history.

Table S5: Robustness audit. The perturbation is applied before exact recentering and local whitening. All calculations use seed 20260806 and IEEE-754 binary64 arithmetic.

ϵ	Samples	Pass fraction	Min. raw Gram singular value	Max. $\lvert Q_\kappa G_\kappa \rvert$
0.00	200	1.000	5.656854	4.07×10^{-16}
0.02	200	1.000	5.396872	4.69×10^{-16}
0.05	200	1.000	4.936776	4.14×10^{-16}
0.10	200	1.000	4.352657	3.31×10^{-16}
0.20	200	1.000	2.940093	3.92×10^{-16}
0.30	200	1.000	0.740439	4.28×10^{-16}

S10 Nonlinear consistency benchmarks and the torsion boundary

Within Assumption S6.1, the covariance completion selects a leading nonlinear Einstein representative in the restricted class. The Bianchi-I and Gowdy sectors below check the constrained variables and normalization on nontrivial reduced solutions. They are not strong-field evidence, do not establish black-hole dynamics, and do not remove the ambiguities listed in Sec. S6.4.

For homogeneous positive $q(\tau)$, let $A = q^{-1}\dot{q}$. The induced-completion Bianchi-I phase is

$$S_{\mathrm{BI}} = \frac{c^3}{64\pi G_{\mathrm{match}}} \int \mathrm{d}\tau \, [\mathrm{Tr}(A^2) - (\mathrm{Tr}\, A)^2]. \tag{S140}$$

The lapse constraint gives $\mathrm{Tr}(A^2) - (\mathrm{Tr}\, A)^2 = 0$, reproducing the Kasner condition. A positive affine state-space metric would remain nonzero and cannot replace this constrained phase; the distinction is supplied here by Theorem S4.1, not by a bare Einstein coefficient.

For unpolarized Gowdy fields (P, Q), the two-polarization action is the hyperbolic wave-map reduction with overall coefficient $c^3/(16\pi G_{\mathrm{match}})$. The remaining longitudinal metric function is reconstructed from first-order constraints, and the integrability condition is a linear combination of the two wave-map equations. This provides a nonlinear two-polarization benchmark, not a general strong-field proof.

The theorem itself concerns the spin-saturated, torsion-free tensor branch. No Einstein–Cartan induction theorem is claimed. If one enlarges the provisional classical source space to an independent spin connection and supplies a Lorentz-spin current, the standard first-order representative permits

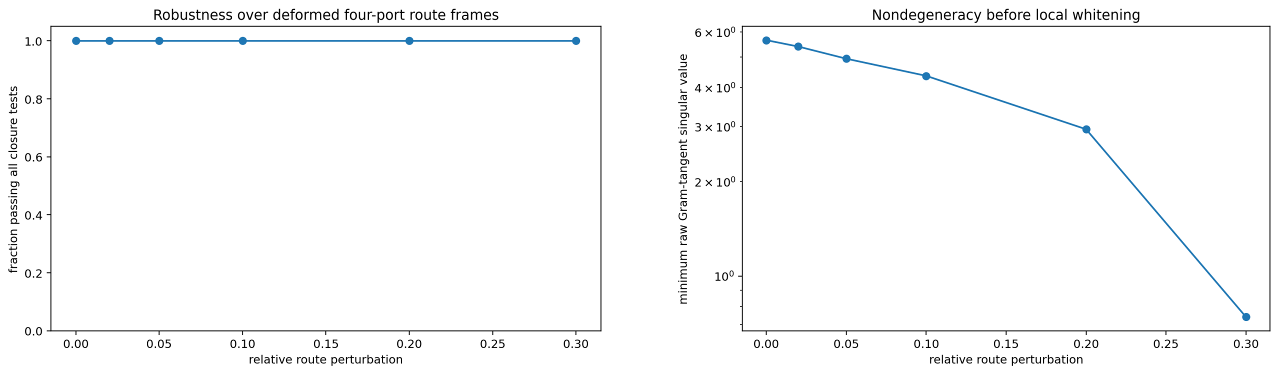

(a) Joint closure pass fraction.

(b) Minimum singular value of the raw Gram tangent before whitening.

Figure S6: The leading relational geometry, mode count, and positive spectral structure are stable throughout the tested nondegenerate route family. BCC specificity first reappears in the exact finite band and quartic angular harmonic.

algebraic Einstein–Cartan torsion [28, 29]; however, the microscopic history has not yet fixed the coefficients of Holst, Nieh–Yan, torsion-squared, or other first-order terms, and it has not generated a quantum connection measure. Fermionic determinants on Riemann–Cartan backgrounds can produce precisely such additional structures [30]. Accordingly, torsion is a schematic extension and an open coefficient problem, not part of Theorem S0.1.

S11 Phenomenology and decisive tests

The model does not predict an absolute laboratory frequency until the event length a and physical event-volume factor η are selected. Its strongest present predictions are therefore correlated shapes and scale-free relations, not standalone numerical frequencies.

S11.1 Correlated continuum observables

The helicity-common tensor phase in Eq. (S134), the first pair threshold in Eq. (S119), and the effective normalization in Eq. (S96) are not independent parameters. Two especially direct model-level sum rules are

$$\frac{\Omega_{\mathrm{pair}} L_g}{c} = 2m\sqrt{\Gamma_{\mathrm{ind}}(m)}, \tag{S141}$$

$$\frac{\hbar G_{\mathrm{match}} \Omega_{\mathrm{pair}}^2}{c^5} = \frac{\eta m^2}{8\pi z_{\mathrm{cell}}(m)}. \tag{S142}$$

The first eliminates the unknown event length completely. The second also eliminates a but retains the physical event-volume factor η; it is therefore scale free but not normalization free. A phenomenological analysis that fits dispersion, threshold, and gravitational normalization independently would not be testing this minimal model.

The continuum signatures are:

1. both helicities acquire the same subluminal f^3 propagation phase with the cubic angular factor in Eq. (S134); quartic birefringence rejects the parity-completed branch;
2. below the first occupied threshold the conservative dressing is nonzero but the zero-temperature pair noise vanishes; dissipation and positive noise begin together;

3. a scalar, vector, or free torsion wave below threshold rejects the minimal constraint complex;
4. a negative physical noise eigenvalue, negative geometry-visible residue, or noninterlacing subthreshold pole rejects the occupied history.

A null gravitational-wave result constrains only the relevant coherent-frame or domain-averaged combination of $a^2\Gamma_{\mathrm{ind}}$; it does not separately determine a, m, η, $\mathcal{Z}_{\mathrm{occ}}$, the pair threshold, or the observed Newton constant.

S11.2 Programmable finite-network protocol

The finite theorem can be tested without identifying the network with spacetime. The compact experiment treats one momentum sector and reuses the complementary-route register while summing the eight transition channels classically.

S11.2.1 Logical registers and state preparation

The five logical qubits are: response ancilla a, Weyl spin s, recurrence r, parity p and Julia complement j. Direct synthesis prepares the occupied two-level lines using three entanglers and calibrated single-qubit rotations. This is the recommended production route because the occupied eigenvectors are analytically known. An eight-step adiabatic continuation, adding 48 entanglers, is retained as an independent preparation check. Phase estimation is unnecessary for the primary experiment but can validate the quasienergy ordering on a larger register.

The response circuit implements a forward finite tick U, an ancilla-selected weak relative-cofactor drive D_+ or D_-, the inverse tick $U^\dagger$, and ancilla readout. Ancilla X and Y contrasts give the real and imaginary linear-response components. For the symmetrized noise, an ancilla Ramsey sequence inserts the same Pauli-resolved source at two times. A nine-qubit two-copy covariance circuit is an alternative when coherent time ordering is less accurate than parallel state preparation.

S11.2.2 Logical and architecture-aware resources

The direct-preparation closed-time-path schedule contains 57 native entanglers and 117 single-qubit rotations on an all-to-all gate set, with estimated entangling depth 39. A declared T-connected five-qubit superconducting patch requires 123–154 native entanglers and depth 72–96 after routing. The dynamic implementation uses eight mid-circuit measurement/reset operations per transition batch. The estimates include the occupied-line preparation, forward and inverse ticks, weak drive, ancilla control and transition batching; they exclude vendor-specific pulse optimization.

Table S6: Architecture-aware resource ledger for one momentum and drive point.

Resource	Declared estimate
Logical register	5 qubits
All-to-all native entanglers	57; entangling depth 39
T-connected superconducting patch	123–154 entanglers; depth 72–96
Single-qubit rotations	117
Mid-circuit measurement/reset	8 per dynamic transition batch
Direct occupied-state preparation	3 entanglers
Adiabatic validation preparation	48 additional entanglers
Two-copy covariance alternative	9 qubits

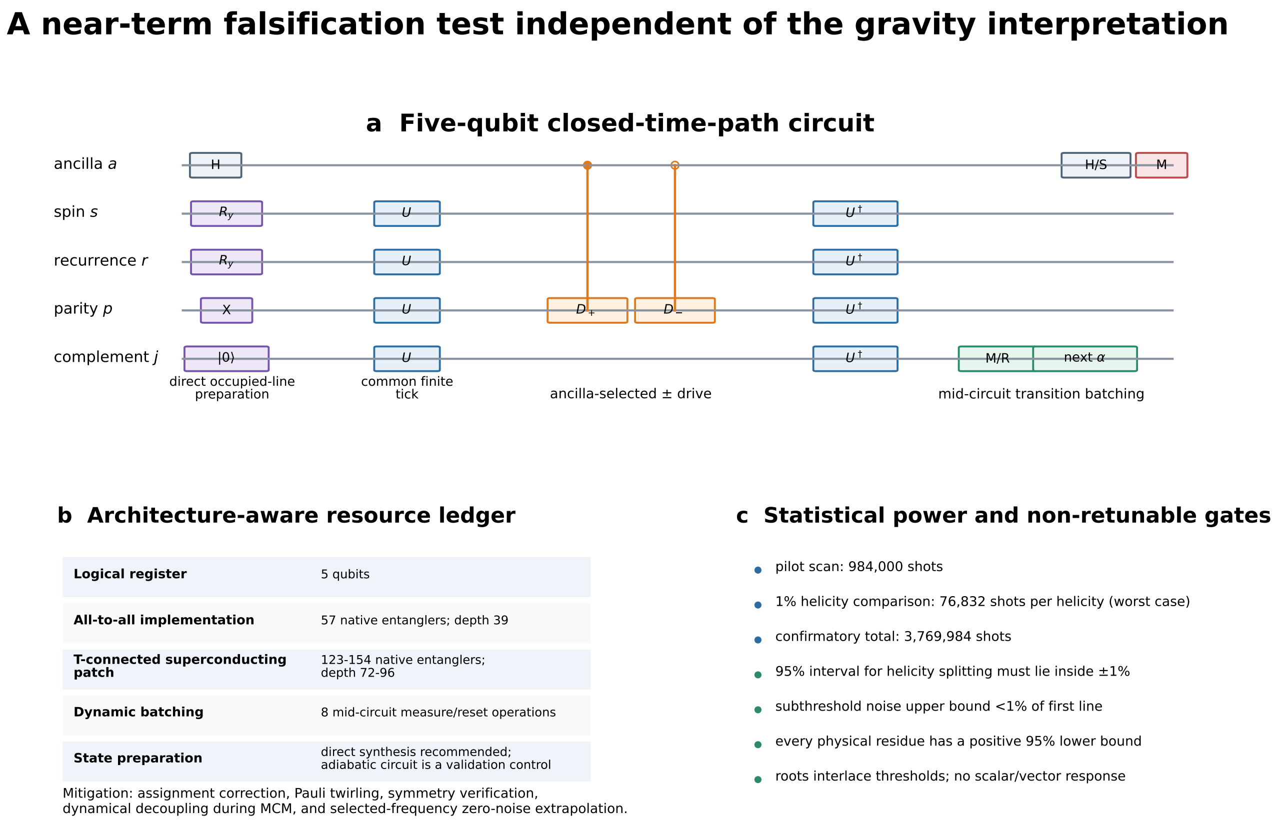

Figure S7: Programmable protocol, architecture-aware resource estimates and the non-retunable statistical gates. The circuit diagram is a logical schedule; hardware transpilation remains platform dependent.

All-to-all trapped-ion processors support arbitrary pairing, parameterized two-qubit rotations, mid-circuit measurement/reset and conditional operations. Dynamic superconducting circuits provide mid-circuit measurement, feed-forward and reset, but measurement-induced crosstalk must be characterized in situ. The mitigation plan therefore includes assignment-matrix correction, four Pauli-twirled compilations at fixed total shots, occupied/parity symmetry verification, dynamical decoupling during mid-circuit measurement and three-scale zero-noise extrapolation at nine selected frequencies.

S11.2.3 Statistical power and acceptance gates

A 41-frequency pilot scan with six circuits and 4,000 shots per circuit uses 984,000 shots. That pilot is not sufficient by itself to certify a 1% helicity bound. A worst-case two-sample 95% interval of width 1% requires 76,832 shots per helicity; a 2% interval requires 19,208. The declared confirmatory budget is

$$3{,}769{,}984 \text{ shots,} \tag{S143}$$

comprising 921,984 helicity-comparison shots, 400,000 quiet-window shots, 160,000 residue shots, 160,000 scalar/vector controls, 1,080,000 selected-frequency zero-noise-extrapolation shots, 64,000 readout-calibration shots and the pilot scan.

The implementation passes only if:

1. the full 95% interval for plus/cross splitting lies inside $[-1\%, 1\%]$;
2. the 95% upper bound on subthreshold noise is below 1% of the first resolved threshold line;

3. every fitted physical residue has a positive 95% lower bound;
4. every geometry-visible root interlaces adjacent distinct pair thresholds;
5. a transverse-tensor drive produces no statistically resolved scalar or vector response.

Bootstrap intervals are formed over independently compiled circuits and shots. Unequal parity occupation, absolute-cofactor transport and a deliberately reduced gap are destructive controls. A failure of any gate rejects the finite implementation before a gravitational interpretation is considered.

S11.2.4 Transfer to other constrained quantum systems

The same protocol family can replace the BCC tick by another finite unitary and the Gram source by any experimentally addressable positive chart. The required observables are the rank of the protected quotient, degeneracy of its response eigenchannels, support of the noise spectrum and sign/interlacing of physical residues. This makes the experiment a general test of relationally protected response in engineered gauge, topological and elastic systems.

S12 Limitations and interpretation

The construction deliberately stops at the level needed to decide the protection question: an exact finite complex, a positive quantum chart and its controlled Gaussian feedback. This establishes a reusable finite theorem while leaving a systematic next expansion.

1. **Controlled Gaussian leading order.** The quantum Gram operators, their covariance and the exact Gaussian Schur feedback are explicit and sufficient to protect the quotient and spectral measure. Non-Gaussian Gram–route entanglement, topology change and an anomaly-free operator constraint algebra define the next expansion.
2. **Conditional nonlinear completion.** The constraint-square theorem, Gaussian stability, finite-kernel matching invariants and direct static branch do not use HKT/Deser. A unique nonlinear Einstein representative still follows only within Assumption S6.1 and modulo Sec. S6.4.
3. **Matter dictionary.** The direct static equation fixes the gravitational normalization but not the map from the displayed cell source ε to realistic composite matter. The recurrence cell is not a derivation of the Standard Model or observed masses.
4. **Event scale and volume.** Equation (S102) contains a and the physical event-volume factor η. The finite model supplies scale-free relations but does not select the absolute laboratory scale.
5. **Representative-specific ultraviolet structure.** Rank, quotient dimension and Stieltjes positivity are open-neighborhood properties. The exact BCC band, cubic harmonic, microscopic tick and domain history are representative dependent.
6. **Near-threshold antiresonances.** Gaussian Gram feedback can create zeros of the corrected propagator immediately below a pair threshold. They are poles of the effective inverse kernel, not additional excitations. The original massless pole, its residue and the one-pole noise-quiet spectrum remain unchanged at this order.
7. **Global dynamics.** Black holes, cosmology, unrestricted strong fields and a complete quantum connection sector require separate analyses.

The conceptual conclusion is nevertheless general: a positive microscopic quantum metric need not reproduce the indefinite scalar part of an off-shell gravitational representative. The correct demand is a positive response on explicit quantum coordinates, an exact relational complex, and spectral health after reduction. The BCC construction proves that this package is nonempty and the Gaussian calculation shows that it is stable to the first quantum correction.

S13 Conclusion

The finite model implements a reusable route from positive quantum distinguishability to physical massless spin-2 dynamics. Six Gauss-invariant Gram coordinates have a positive full-rank susceptibility. Three event-section directions and one scalar constraint reduce them to two tensor classes. The positive occupied kernel and Fierz–Pauli representative differ by a constraint square, so the indefinite scalar never becomes a negative-norm particle.

The leading quantum correction is also controlled. Integrating the Gram fluctuation yields an exact parallel-sum propagator that preserves the original massless roots, their residues, the rank-two quotient and the complete spectral measure. The exact finite kernel fixes the quartic directional harmonic and threshold–dispersion relations independently of nonlinear uniqueness, while constraint propagation fixes the same normalization in a direct BCC inverse-distance branch.

The resulting design principle is broader than the BCC representative: build positive quantum coordinates, prove the relational complex exactly, reduce before counting particles, and match the full finite spectral kernel before truncating it. A programmable five-qubit test can reject this principle in the displayed realization without requiring a gravitational experiment.

S14 Finite quantum Gram collective chart

For the cutoff $K = 4$, the eight Schwinger modes have total boson-number sectors $N = 0, 2, 4$ of raw dimensions 1, 36, and 330. Diagonalizing $\widehat{\boldsymbol{J}}^2_{\text{tot}}$ gives Gauss-singlet dimensions 1, 6, and 20, respectively. In their direct sum, the maximally mixed state has the centered mean Gram matrix

$$\bar{\mathcal{G}} = \begin{pmatrix} 3/4 & -1/4 & -1/4 & -1/4 \\ -1/4 & 3/4 & -1/4 & -1/4 \\ -1/4 & -1/4 & 3/4 & -1/4 \\ -1/4 & -1/4 & -1/4 & 3/4 \end{pmatrix}, \qquad \operatorname{spec}(\bar{\mathcal{G}}) = (0, 1, 1, 1). \tag{S144}$$

In the chart ordering of Eq. (S31), the exact symmetrized covariance is

$$\chi = \begin{pmatrix} 5/9 & -19/216 & -19/216 & -19/216 & -5/27 & -5/27 \\ -19/216 & 5/9 & -19/216 & -19/216 & -5/27 & 59/432 \\ -19/216 & -19/216 & 5/9 & -19/216 & 59/432 & -5/27 \\ -19/216 & -19/216 & -19/216 & 5/9 & 59/432 & 59/432 \\ -5/27 & -5/27 & 59/432 & 59/432 & 61/216 & -7/144 \\ -5/27 & 59/432 & -5/27 & 59/432 & -7/144 & 61/216 \end{pmatrix}. \tag{S145}$$

Its leading principal minors are

$$\frac{5}{9}, \frac{14039}{46656}, \frac{792161}{5038848}, \frac{18799333}{241864704}, \frac{921167317}{104485552128}, \frac{45137198533}{60183678025728}, \tag{S146}$$

all strictly positive. The numerical eigenvalues are

$$(0.0425534,\ 0.129577,\ 0.304249,\ 0.643519,\ 0.822179,\ 0.844960). \tag{S147}$$

This proves the finite local invertibility used in Proposition S2.2. The calibration state is a convenient exact trace state, not a derived physical vacuum.

S15 BCC identities and primitive volume

The eight routes obey

$$\frac{1}{8}\sum_{\boldsymbol{r}\in\mathcal{R}} r_i r_j = \delta_{ij}. \tag{S148}$$

For $\theta_{\boldsymbol{r}} = \boldsymbol{r}\cdot\boldsymbol{q}/2$,

$$\frac{1}{8}\sum_{\boldsymbol{r}} 4\sin^2\theta_{\boldsymbol{r}} = 2(1-\cos q_x\cos q_y\cos q_z). \tag{S149}$$

The determinant of the primitive basis $(\boldsymbol{r}_1,\boldsymbol{r}_2,\boldsymbol{r}_3)$ is four, proving (S101). The BCC network contains multiple finite-band valleys; the present theorem concerns the principal history sector retained by the local history register rather than a nonlocal momentum projection.

S16 Centered-Gram tangent and curvature record

At the identity coframe, a symmetric strain h changes the cofactor metric by

$$\delta C = 2[(\operatorname{Tr} h)I - h]. \tag{S150}$$

Consequently,

$$\delta\mathcal{G}(h) = 2T[(\operatorname{Tr} h)I - h]T^T. \tag{S151}$$

The inverse on the centered six-dimensional space is

$$h = \frac{9}{64}\operatorname{Tr}(T^T\delta\mathcal{G}T)I - \frac{9}{32}T^T\delta\mathcal{G}T. \tag{S152}$$

For the ten spacetime bivectors collected as columns of P, the tetrahedral/normal frame obeys $PP^T = I_6$. Thus P^T is the Moore–Penrose inverse of the measurement map. Riemann pair symmetry makes the curvature operator symmetric on bivectors, while the algebraic Bianchi identity removes one mixed component, leaving twenty algebraic curvature components.

S17 Constrained representative calculation

For $\boldsymbol{\kappa} = (0,0,\kappa)$,

$$Q_\kappa h = -\kappa^2(h_{11}+h_{22}), \tag{S153}$$

and the event-section image contains the 13, 23, and 33 directions. The scalar representative is proportional to $q_\kappa = \operatorname{diag}(-\kappa^2,-\kappa^2,0)$, with $\|q_\kappa\|^2 = 2\kappa^4$. The two survivors are plus and cross. Equation (S68) follows immediately from $K_+ - K_{\mathrm{FP}} = 3\mathcal{Z}_{\mathrm{occ}}p^2\Pi_Q$.

S18 Finite-band coefficients and residue sign

Each port contribution decomposes as

$$4A_{\boldsymbol{r}}\frac{s_{\boldsymbol{r}}^2 - x}{G_{\boldsymbol{r}}^2 - x} = 4A_{\boldsymbol{r}} - \frac{4A_{\boldsymbol{r}}(G_{\boldsymbol{r}}^2 - s_{\boldsymbol{r}}^2)}{G_{\boldsymbol{r}}^2 - x}. \tag{S154}$$

Since $G_{\boldsymbol{r}} > |s_{\boldsymbol{r}}|$ for $\Delta > 0$, all Stieltjes weights are positive. For a positive-frequency root $x_n = \nu_n^2 < 4$,

$$\mathcal{R}_n = -\frac{1}{2\nu_n\sqrt{1-\nu_n^2/4}\,K'(x_n)} > 0. \tag{S155}$$

At $\boldsymbol{q} = 0$, the massless root is exact. For $\boldsymbol{q}\neq 0$, $K(0) > 0$ and the first left-hand pole limit is negative, yielding one low root.

Table S7: Representative reproducibility checks for the hybrid induction result. The fitted coefficient is obtained independently from small-momentum finite differences of the occupied metric.

Check	Result
Max. Weyl-shell identity residual	5.55×10^{-16}
Max. recurrence-block unitarity residual	4.44×10^{-16}
Max. Julia-block unitarity residual	2.22×10^{-16}
Gauss-singlet dimensions at $N = 0, 2, 4$	$1, 6, 20$
Quantum Gram covariance rank	6 (exact positive minors)
Relative residual of fitted z_{cell}	1.43×10^{-8}
Constraint-square identity, 500 random tests	7.11×10^{-15}
Gravity–threshold sum rule	0.0
Low-pole remainder power after quartic subtraction	5.948
Deformed-route closure tests	1200/1200 passed
Gaussian corrected susceptibility rank	6 for every tested q
Fluctuating-coframe projector tests	4000/4000 rank two
Gaussian feedback residues	all positive
Static $1/\pi$ coefficient fit error	1.08×10^{-7}

S19 Audit and reproducibility

The source package contains the complete manuscript, figures, the response script `induced_gravity_audit_v2_3.py`, and the quantum collective-coordinate script `quantum_gram_collective_audit_v2_3.py`, together with `quantum_gram_backreaction_audit_v1_0.py`, `static_bcc_response_audit_v1_0.py`, and `circuit_resource_audit_v1_0.py`. The script evaluates the exact BCC Weyl and recurrence unitarity identities, the canonical Julia dilation, the microscopic induced coefficient, primitive event-volume convention, exact low pole, directional sixth-order remainder, centered-Gram rank, constraint cohomology, route whitening, Stieltjes weights, residues, and the open-neighborhood route audit. It writes the machine-readable report `induced_gravity_audit_v2_3.json`. The path-closure calculation is supplied as `path_closure/structural_audit.py`. The response and path audits use fixed seed 20260806 and NumPy/SciPy IEEE-754 binary64 arithmetic; the quantum Gram audit is deterministic and also reports exact rational covariance minors. Numerical residuals near 10^{-14} indicate double-precision closure, not symbolic zero.

Data and code availability

All scripts, machine-readable reports, and figure-generation outputs needed for the numerical statements in this article are supplied as Supplemental Material. The primary command is

```
python induced_gravity_audit_v2_3.py
```

and requires Python 3, NumPy, SciPy, and Matplotlib; exact package requirements and expected file hashes are listed in `SUPPLEMENT_README.md` and `requirements.txt`. The quantum Gram calibration is run with

```
python quantum_gram_collective_audit_v2_3.py
```

and the separate path-closure audit is run from the `path_closure/` directory. The Gaussian back-reaction, static Green-function and resource audits are run from `audit_v2/`. The supplement contains the scripts, JSON outputs, execution logs, and checksums used for the reported calculations. No permanent repository identifier is claimed in the manuscript; one may be added upon archival deposit.

References

[1] A. D. Sakharov, "Vacuum quantum fluctuations in curved space and the theory of gravitation," Sov. Phys. Dokl. **12**, 1040 (1968) [Dokl. Akad. Nauk SSSR **177**, 70 (1967)].

[2] M. Visser, "Sakharov's induced gravity: a modern perspective," Mod. Phys. Lett. A **17**, 977 (2002), arXiv:gr-qc/0204062.

[3] S. Weinberg, "Photons and gravitons in perturbation theory: derivation of Maxwell's and Einstein's equations," Phys. Rev. **138**, B988 (1965).

[4] S. Deser, "Self-interaction and gauge invariance," Gen. Relativ. Gravit. **1**, 9 (1970), arXiv:gr-qc/0411023.

[5] C. Teitelboim, "How commutators of constraints reflect the spacetime structure," Ann. Phys. **79**, 542 (1973).

[6] S. A. Hojman, K. Kuchař, and C. Teitelboim, "Geometrodynamics regained," Ann. Phys. **96**, 88 (1976).

[7] D. Lovelock, "The Einstein tensor and its generalizations," J. Math. Phys. **12**, 498 (1971).

[8] G. M. D'Ariano and P. Perinotti, "Derivation of the Dirac equation from principles of information processing," Phys. Rev. A **90**, 062106 (2014), arXiv:1306.1934.

[9] A. Bisio, G. M. D'Ariano, P. Perinotti, and A. Tosini, "Weyl, Dirac and Maxwell quantum cellular automata," Found. Phys. **45**, 1203 (2015), arXiv:1601.04842.

[10] P. Raynal, "Simple derivation of the Weyl and Dirac quantum cellular automata," Phys. Rev. A **95**, 062344 (2017), arXiv:1703.05890.

[11] T. Regge, "General relativity without coordinates," Nuovo Cimento **19**, 558 (1961).

[12] B. Bahr and B. Dittrich, "(Broken) gauge symmetries and constraints in Regge calculus," Class. Quantum Grav. **26**, 225011 (2009), arXiv:0905.1670.

[13] V. Bonzom and B. Dittrich, "Dirac's discrete hypersurface deformation algebras," Class. Quantum Grav. **30**, 205013 (2013), arXiv:1304.5983.

[14] F. Conrady and L. Freidel, "On the semiclassical limit of 4-dimensional spin foam models," Phys. Rev. D **78**, 104023 (2008), arXiv:0809.2280.

[15] S. K. Asante, B. Dittrich, and H. M. Haggard, "Effective spin foam models for four-dimensional quantum gravity," Phys. Rev. Lett. **125**, 231301 (2020), arXiv:2004.07013.

[16] B. Dittrich and A. Kogios, "From spin foams to area metric dynamics to gravitons," Class. Quantum Grav. **40**, 095011 (2023), arXiv:2203.02409.

[17] T. A. Brun and L. Mlodinow, "Quantum electrodynamics from quantum cellular automata, and the tension between symmetry, locality and positive energy," Entropy **27**, 492 (2025), arXiv:2503.05998.

[18] A. F. Jercher, J. D. Simão, and S. Steinhaus, "$(2+1)$ Lorentzian quantum cosmology from spin foams: opportunities and obstacles for semiclassicality," Class. Quantum Grav. **42**, 085015 (2025), arXiv:2411.08109.

[19] A. Calcinari, A. Delhom, and D. Oriti, "Collective excitations in quantum gravity condensates," arXiv:2605.18977.

[20] H. C. Steinacker, "Modified gravity at large scales on quantum spacetime in the IKKT model," arXiv:2601.08031.

[21] B.-L. Hu and E. Verdaguer, "Stochastic gravity: theory and applications," Living Rev. Relativ. **11**, 3 (2008), arXiv:0802.0658.

[22] I. Klich, "Full counting statistics: an elementary derivation of Levitov's formula," in *Quantum Noise in Mesoscopic Physics*, edited by Y. V. Nazarov (Springer, 2003), pp. 397–402, arXiv:cond-mat/0209642.

[23] R. P. Feynman and F. L. Vernon, "The theory of a general quantum system interacting with a linear dissipative system," Ann. Phys. **24**, 118 (1963).

[24] L. V. Keldysh, "Diagram technique for nonequilibrium processes," Sov. Phys. JETP **20**, 1018 (1965).

[25] M. Fierz and W. Pauli, "On relativistic wave equations for particles of arbitrary spin in an electromagnetic field," Proc. R. Soc. Lond. A **173**, 211 (1939).

[26] V. A. Kostelecký and M. Mewes, "Testing local Lorentz invariance with gravitational waves," Phys. Lett. B **757**, 510 (2016), arXiv:1602.04782.

[27] C. Gong, T. Zhu, R. Niu, Q. Wu, J.-L. Cui, X. Zhang, W. Zhao, and A. Wang, "Gravitational wave constraints on non-birefringent dispersions of gravitational waves due to Lorentz violations with GWTC-3," Phys. Rev. D **107**, 124015 (2023), arXiv:2302.05077.

[28] T. W. B. Kibble, "Lorentz invariance and the gravitational field," J. Math. Phys. **2**, 212 (1961).

[29] F. W. Hehl, P. von der Heyde, G. D. Kerlick, and J. M. Nester, "General relativity with spin and torsion: foundations and prospects," Rev. Mod. Phys. **48**, 393 (1976).

[30] J. R. Nascimento, A. Yu. Petrov, and P. J. Porfirio, "Induced gravitational topological term and the Einstein–Cartan modified theory," Phys. Rev. D **105**, 044053 (2022), arXiv:2108.05705.

[31] A. Barbieri, "Quantum tetrahedra and simplicial spin networks," Nucl. Phys. B **518**, 714 (1998), arXiv:gr-qc/9707010.

[32] J. C. Baez and J. W. Barrett, "The quantum tetrahedron in three and four dimensions," Adv. Theor. Math. Phys. **3**, 815 (1999), arXiv:gr-qc/9903060.

[33] E. Bianchi, P. Dona, and S. Speziale, "Polyhedra in loop quantum gravity," Phys. Rev. D **83**, 044035 (2011), arXiv:1009.3402.

[34] R. Arnowitt, S. Deser, and C. W. Misner, "The dynamics of general relativity," Gen. Relativ. Gravit. **40**, 1997 (2008), arXiv:gr-qc/0405109.

[35] G. S. Joyce, "On the simple cubic lattice Green function," J. Phys. A **5**, L65–L68 (1972).

[36] J. W. York Jr., "Conformally invariant orthogonal decomposition of symmetric tensors on Riemannian manifolds and the initial-value problem of general relativity," J. Math. Phys. **14**, 456–464 (1973).

[37] M. Iqbal et al., "Non-Abelian topological order and anyons on a trapped-ion processor," Nature **626**, 505–511 (2024).

[38] E. Bäumer et al., "Quantum Fourier transform using dynamic circuits," Phys. Rev. Lett. **133**, 150602 (2024).

[39] A. Carrera Vazquez et al., "Combining quantum processors with real-time classical communication," Nature **636**, 75–79 (2024).

[40] B. S. DeWitt, "Quantum theory of gravity. I. The canonical theory," Phys. Rev. **160**, 1113 (1967).

[41] D. Hothem *et al.*, Measuring error rates of mid-circuit measurements, *Nat. Commun.* **16**, 5761 (2025).

[42] A. Ransford *et al.*, A 98-qubit trapped-ion quantum computer with all-to-all connectivity, *Nature* **655**, 81–86 (2026).